TUM School of Natural Sciences

TECHNISCHE UNIVERSITÄT MÜNCHEN

Fakultät für Physik

Master Thesis

Cluster Characterization and Alignment Strategies for Cylindrically Bent MAPS Detectors

Christopher Ehrich

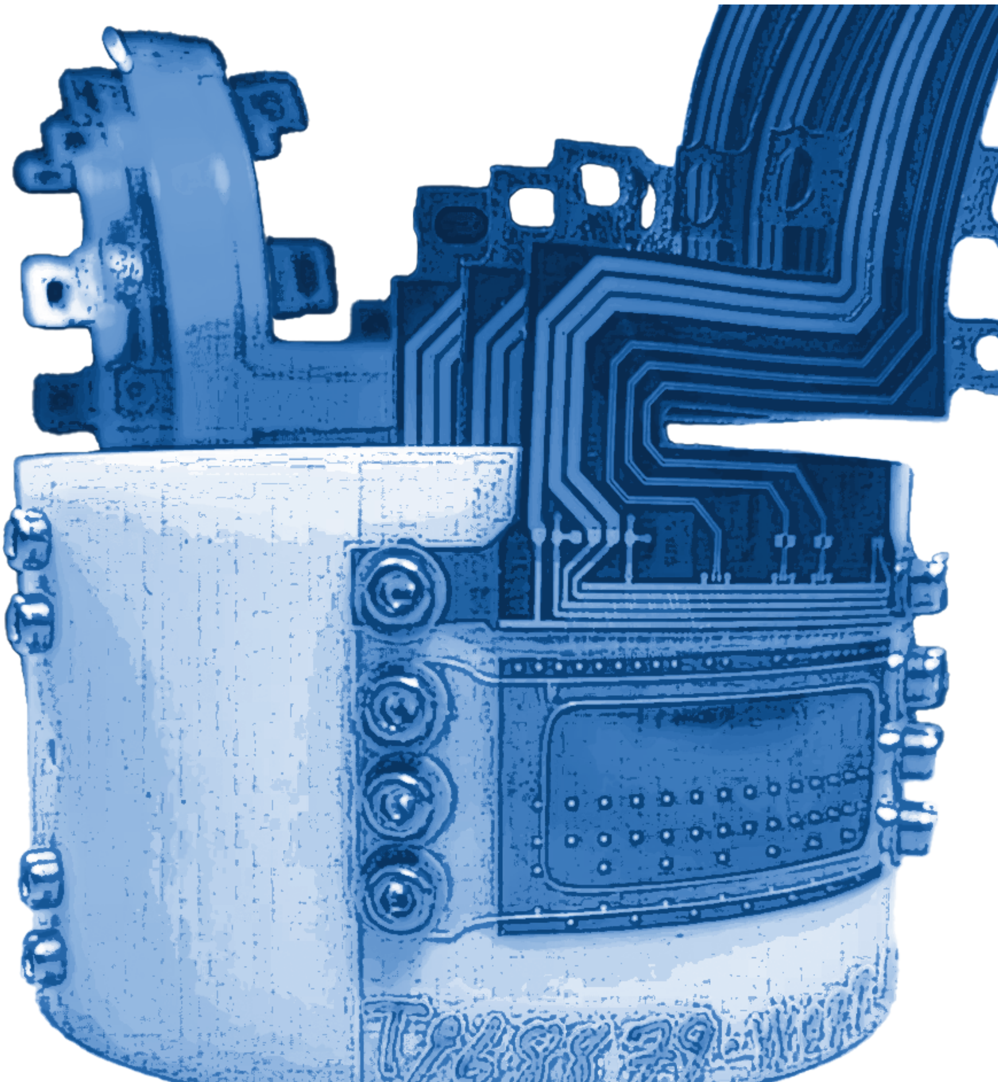

TECHNISCHE UNIVERSITÄT MÜNCHEN

TUM School of Natural Sciences

Fakultät für Physik

Cluster Characterization and Alignment Strategies for Cylindrically Bent MAPS Detectors

Charakterisierung des Cluster-Verhaltens und Ausrichtungsstrategien für zylindrisch gebogene MAPS-Detektoren

Master Thesis

Author: Christopher Ehrich
Examiner: Prof. Dr. Laura Fabbietti
Supervisor: Berkin Ulukutlu
Advisor: Dr. Roman Gernhäuser

Date: 16.11.2023

I confirm that the results presented in this master's thesis is my own work and I have documented all sources and materials used.

Ich versichere, dass ich diese Masterarbeit selbstständig verfasst und nur die angegebenen Quellen und Hilfsmittel verwendet habe.

Garching, 16.11.2023 Christopher Ehrich

Abstract

The upgrade of the ALICE detector's Inner Tracking System (ITS3) is a very ambitious project that plans to redesign the detection layers of the inner barrel using wafer-scale bent chips. Studies must be carried out to ensure that the planned detector can operate to the desired specifications and demonstrate the performance of bent chips in realistic experimental physics conditions. Towards this goal, studies were conducted in the scope of this thesis using a small telescope featuring bent ALice PIxel DEtector (ALPIDE) chips (the sensors employed at the existing ITS2). The investigations conducted include clustering behavior in bent Monolithic Active Pixel Sensors (MAPS) detecting low momentum (<GeV) particles, correlations between energy deposition and particle momentum, and alignment strategies for cylindrically bent detector geometry.

The clustering behavior of bent MAPS was evaluated using proton beams of different energies impinging on a polypropylene fiber target. With proton-proton elastic scattering as the dominant reaction channel, this results in a well-defined coincidence pattern of the outgoing particles. Data sets were taken using different signal thresholds of 100e, 200e, and 300e charge equivalent. Through the special target geometry and the reaction pattern, different alignment strategies for cylindrically bent detectors were developed and qualified based on the time to converge, the best distance of the closest approach (DCA), and the opening angle calculated in the aligned configurations.

Contents

1 Introduction

This chapter gives an overview of the ALICE experiment, discussing the collisions, a brief description of the LHC, the physics goals of the experiment, and a description of the instrumentation at ALICE. Following the section on ALICE, background on ALPIDE chips used for tracking is given, which will discuss the properties of the chips and the innovations they brought with them to the previous upgrade (ITS2). The coming upgrade to the ALICE inner tracking system (ITS3) and the innovations follow in the next section.

1.1 ALICE

ALICE (A Large Ion Collider Experiment) is a detector dedicated to heavy-ion physics at the Large Hadron Collider (LHC). Due to the large center of mass energies in one collision, a huge number of outgoing particles is created in a single event, and all the detector systems have to cope with this special feature. ALICE as of LHC Run 3 measures Pb-Pb, and p-p collisions at center of mass energy per nucleon pair $\sqrt{s_{NN}} =$ 5.36 TeV/[1], and 13.6 TeV[2] respectively producing thousands of particles in a small volume. Quark Gluon Plasma (QGP), a state of matter predicted to have existed briefly after the Big Bang, is formed and studied in these collisions with the goal of understanding the nuclear equation of state and the nature of the strong force [3]. The ALICE detector is specialized for the high multiplicities and low momentum of the particles produced in these heavy ion collisions.

The LHC is the final accelerator of a chain of accelerators that, as of run 3, brings beams up to the record energy of 6.8 TeV/Z [4] and is designed for collisions of energies up to 7.0 TeV/Z [3, 4]. In the ALICE experiment, the main focus is on lead-lead collisions. In order to produce lead beams of energy 2.76 TeV/u, lead ions must follow a series of booster accelerators prior to injection at the LHC. First, a purified lead sample is heated to ~500 °C. Lead vapor is ionized by a current up to the charge state Pb^{29+}, which is accelerated to 4.2 MeV/u before it is further ionized to Pb^{54+} by passing through a carbon foil stripper. The Pb^{54+} beam is accelerated to 72 MeV/u at the Low Energy Ion Ring (LEIR), which then transfers the beam to the Proton Synchrotron (PS), which brings the beam up to 5.9 GeV/u. The beam is then sent to the Super Proton Synchrotron (SPS) to strip the ions of remaining electrons with a second foil and accelerate the Pb^{82+} up to 177 GeV/u. This beam is passed on to the LHC, which has two beam pipes, one clockwise and one counterclockwise, which bring the beams up to 2.76 TeV/u and collide them [3].

The LHC is a 27 km circumference collider made up of eight arcs (containing bending magnets) and eight insertions (containing cavities with radiofrequency 400 MHz electric fields synchronized with bunches and providing them with 5 MV/m) [3]. The LHC has four intersection points between two beam pipes corresponding to the four main experiments with their detector apparatuses: CMS, LHCb, ATLAS, and ALICE.

1.1.1 High Energy Physics at ALICE

Cosmologists agree that in the Big Bang, matter came from an extremely hot and dense region of space. In this extreme phase, quarks are close enough together to maintain a neutral color charge, such that individual quarks would be able to freely move across distances larger than their normal confinement space: the size of the nucleon. The ALICE experiment aims to study not only the evolution and properties of this extreme state of matter but also the interaction between particles produced in this very hot and dense environment. Nuclei, for example, are generated in these collisions. If two particles are close in phase space, their interaction can be studied in detail. One mystery in astrophysics, where such investigations are relevant, is the internal composition of neutron stars, where knowledge about how nucleons interact in a very dense environment is crucial.

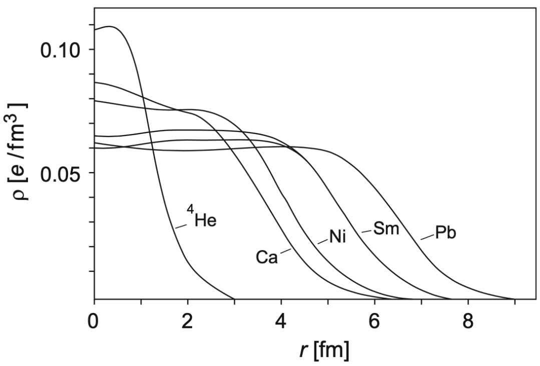

Figure 1.1: Charge Density of the Nucleus from [5]

The nuclear equation of state (EoS) at low energies is understood. The nucleus has a form factor, usually Gaussian or oscillating, corresponding to density profiles that are either Gaussian or spherical with a diffuse edge, respectively [5]. Light nuclei have Gaussian charge and density distributions, but most nuclei have a thin, soft surface but a hard core saturated with nucleons. Sample density profiles are shown in fig. 1.1. The central (saturated) density of the nucleus is about 0.17 nucleons/fm^3[5]. The density is plotted against the radius of nuclei in fig. 1.1, and it can be seen that except for the light He nucleus, nuclear matter saturates in the center and falls off for about 2 fm of skin. Under extreme pressure and temperature, the nuclear matter is expected to undergo a phase transition. Astrophysical observations of neutron stars have confirmed the existence of matter much denser than the nuclear saturation density.

In nuclear physics, particularly in three-body systems, unresolved questions persist, especially regarding the nature of the strong interaction in neutron-rich and dense systems like neutron stars. At heavy ion colliders, densities multiple times the nuclear saturation density are achieved, and it is predicted that the cores of neutron stars are also much denser than nuclear saturation. In such systems, introducing strangeness as an additional degree of freedom may be thermodynamically favorable, depending on the potential of the interaction.

To measure the potential of such interaction, it is useful to employ a technique known as femtoscopy, whereby one uses the statistical correlation of particles measured in the same phase space to calculate the strength of an interaction [6]. It is, in particular, useful to measure not only two and three body nucleon (N−N and N−N−N) potentials but also to measure nucleon-nucleon-hyperon potentials (N−N−Y) [6], where a hyperon is a baryon containing at least one strange quark. Thanks to the proximity of ALICE's inner tracking system (ITS) detectors to the beam collision point, it is possible to track and identify heavy-flavor baryons. The Λ_c^+ is the lowest mass charm baryon. The mean lifetime of no more than $\tau \sim 2 \times 10^{-13}$s) and experimentally determine the potential. At low $p_T \lesssim 1\,\mathrm{GeV/c}$, the lambda hyperon decay length is $\sim 60\,\mu\mathrm{m}$[7]. The original ITS had an impact parameter resolution larger than this, but ITS2 tripled it to about $15\,\mu\mathrm{m}$ for $p_t = 1\,\mathrm{GeV/c}$[8]. The beam pipe of the ITS was decreased from 29.4 mm to 19.8 mm during the ITS2 upgrade, allowing for 9.6 mm closer placement to the collision region of the innermost detector layer and improving the impact parameter resolution so that the $\Lambda_c \longrightarrow pK^-\pi^+$ can be observed[9, 10, 11].

Another aspect of nuclear physics at ALICE is the production of light nuclei in high-energy collisions. In heavy ion collisions, the kinetic energy of the colliding nuclei is transformed into a shower of particles and antiparticles. Statistical hadronization and coalescence models describe the hadronization process from the hot fireballs produced by heavy ion collisions at ALICE. The statistical model treats the fireball as a hadron resonance gas in global chemical equilibrium. The gas expands and cools to a chemical freeze-out, at which point the hadrons stop interacting. Despite the relatively low 2.2 MeV binding energy of deuterium, some nucleons produced in the fireball bind together and survive until chemical freeze-out. This model successfully predicts the hadron and light nuclei yields detected at ALICE [6]. The problem with this thermal model is that every collision has a set of fit parameters that cannot be easily determined. The hadronization in the coalescence model, contrary to the thermal model, assumes that particles can continue interacting even after the fireball produces them. This model assumes nuclei and anti-nuclei are produced when nucleons (or anti-nucleons) are emitted close enough in phase space to form a bound state. This model has also successfully reproduces nuclei and anti-nuclei production from collisions at the LHC[6].

1.1.2 ALICE Detector Overview

Several layers of detectors with different functions surround the central barrel as seen in fig. 1.2. First is the ITS, which tracks the trajectory of charged particles and is under investigation if it can support particle identification (PID) of low momentum particles by calorimetry[13, 14]. These particles can come from the collision point, decays of particles from the collision point, and cosmic rays. Next is the Time Projection Chamber (TPC), which further contributes to the tracking and momentum calculation of charged particles, enabling very precise PID for low-momenta particles by measuring their energy loss in the detector gas volume. The following layer is the Transition Radiation

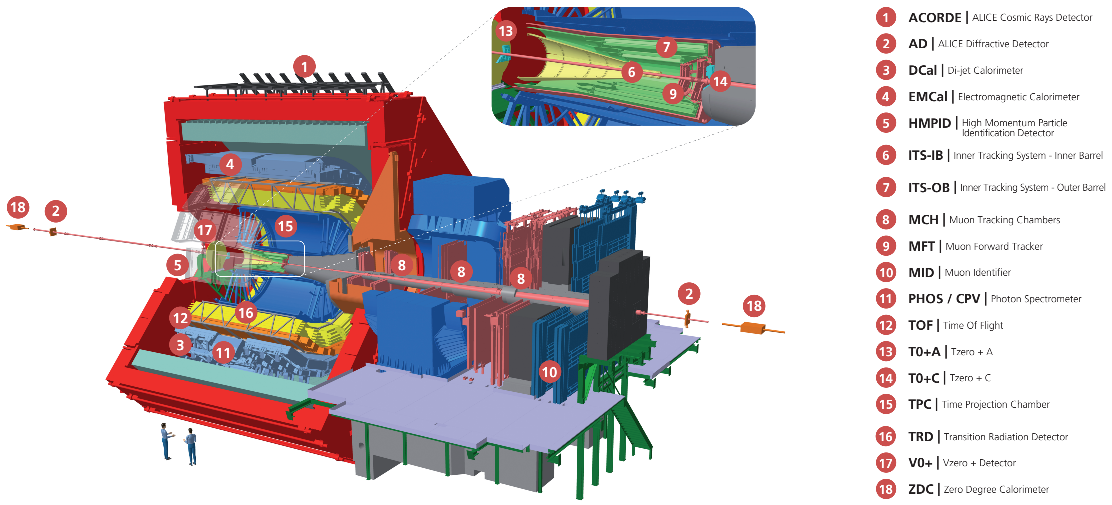

Figure 1.2: The ALICE Detector System taken from [12].

Detector (TRD), which helps with the PID of high-energy electrons. Following is the Time of Flight (TOF) detector, which is used to reconstruct particle velocities. The High Momentum Particle Identification Detector (HMPID) is also installed for high momentum PID.

Along the beam axis is a set of forward detectors. These are used for particles at small angles along the beamline, such as spectator nucleons that did not participate in the production of the hot fireball. These nucleons are detected at the Zero Degree Calorimeter (ZDC). The VZERO (V0) detector measures charged particles and helps with event triggering. The Forward Multiplicity Detector (FMD) informs about the number of charged particles produced along the beam axis.

The Muon Spectrometer is an integral part of ALICE because muons penetrate deeply from within QGP.

The Photon Spectrometer is used to detect photons produced from QGP formation. This includes the Electromagnetic Calorimeter (EMCal), which measures the energy of photons and electrons, and the Di-jet Calorimeter (DCal) for measuring particles coming out of jets, as di-jet events provide useful information to probe QGP. The Photon Multiplicity Detector (PHOS) detects high-energy photons.

1.2 Inner Tracking System

This section will cover the current Inner Tracking System (ITS2), starting with background on the initial upgrade. Next, the working principle of semiconductor detectors is detailed, followed by a description of the system's physical structure. This section will close with the material budget of the inner layers, a critical point in the coming ITS3 upgrade.

During the long LHC shutdown 2 (LS2) 2019-2021, the six layers of the original ITS trackers were replaced with seven new ones organized into three barrels (shown in fig. 1.4) that improved the vertexing (tracing the particles' origin) and tracking performance. The ITS had a two-fold improvement for the impact parameter resolution and tracking efficiency for low transverse momentum particles ($\lesssim$1 GeV/c), as can be seen in fig. 1.10.[15] In addition, the readout capabilities were upgraded to handle Pb–Pb interaction rates of up to 50 kHz demanded after LS2 [15]. ITS2 already has a very high granularity, could withstand higher radiation impact, a reduced material budget, and one more detection layer than the original ITS. This allows for tracking particles at smaller angles and better measurements of observables such as momentum, PID, impact parameters, and vertexing.

The ITS is a semiconductor particle detector. The working principle of such detectors fundamentally comes from atomic physics. In individual atoms, electrons fill discreet energy levels. In an atomic lattice, the energy levels combine to form bands, specifically the valence and conduction bands. Electrons are only shared between neighboring atoms in the valence band, while the conduction band traverses the whole lattice, consisting of free electrons. These two bands overlap in metals but are separated by a band gap in insulators and semiconductors. The energy required to excite an electron from the valence band to the conducting band, known as the band gap, in pure silicon at room temperature 300 k is 1.12 eV [16]. MAPS uses doped silicon, which has an even higher conductivity by changing the number of electron donors and acceptors in the lattice to form a p-n junction [16, p. 590].

Silicon detectors exploit the semiconductor's ability to easily generate electron-hole

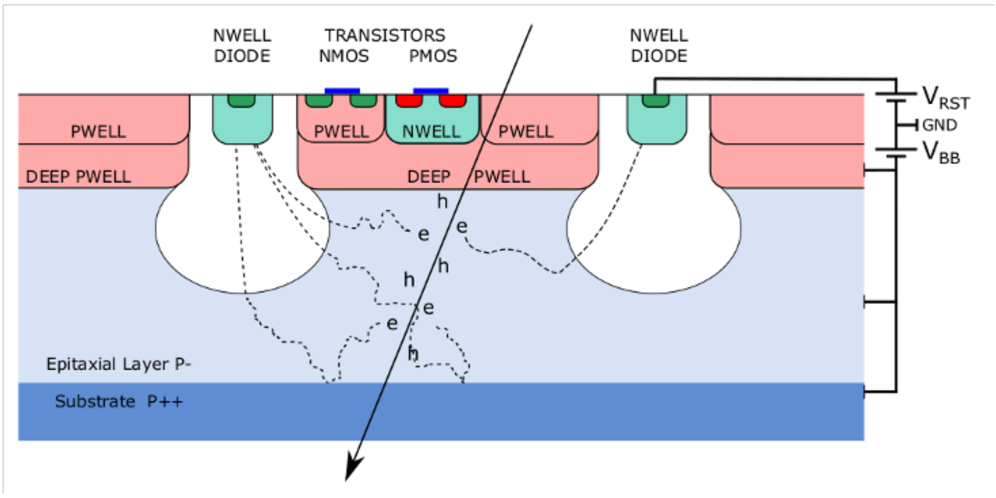

Figure 1.3: Working principle of charge collection in MAPS[17]

pairs through interaction with energetic charged particles. At low temperatures, valence electrons are shared between neighboring silicon atoms; however, thermal excitations are enough to ionize atoms in the lattice, sending valence electrons into the conduction band, which allows them to move freely about the crystal lattice. In addition, effectively, a positively charged particle called a "hole" is left behind by the freed electron, which also moves around and interacts attractively with electrons. However, in the ITS detector implementation, a positively charged collector, the NWELL DIODE, attracts the electrons after they diffuse and get close enough, as shown in fig. 1.3. The diffusion is slow, but when a higher back bias voltage (V_{BB}) is applied, the electrons are accelerated to the collector, speeding up collection time. The voltage of the induced signal, determined by the number of electrons arriving at the collector, must be higher than that of the collection threshold to register as a hit. At ITS, many chips with many pixels are arranged in a grid with known positions. When ionizing radiation passes through the barrels and deposits sufficient energy in the detector layers, simultaneously, many electron-hole pairs are generated, diffused, and collected in the pixels around the neighborhood of the collisions within the chips. No signal is sent from a pixel unless a charge is collected, called zero suppression. During an event, charge collectors send out signals simultaneously, and this data is saved together with the readout from other pixels on all detectors that registered a hit, which provides geometric detail about the path of the radiation, from which tracks can be formed and that trace back towards the point where the particle was produced.

Now that the microscopic function is described, the macroscopic structure of the

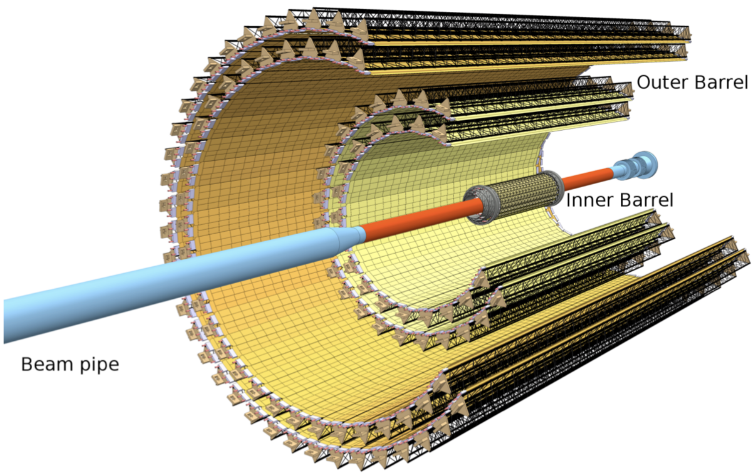

Figure 1.4: Design of the full ITS2 detector: ITS2 has two sets of barrels: the outer barrel with four layers and the inner barrel with three. Each layer comprises modular staves containing ALPIDE sensors and supporting infrastructure that wrap around the beam pipe. taken from [18].

ITS will be discussed. The current inner tracking system, shown in fig. 1.4 has two barrel categories: the inner barrel with three layers of detectors around the beam pipe (surrounding the inner barrel shown in fig. 1.4), and the outer barrel with four layers of detectors. The inner and outer barrels have similar structures. Layers from each barrel are composed of flat segments called staves that wrap around the beam axis [9, 14]. The staves are attached to a half-cylinder support structure to form Half-Layers. The Half-Layer is composed of the following parts: the Space

Frame, Cold Plate, Hybrid Integrated Circuit (IC), Half-Stave, and Module, as seen in fig. 1.5. The Space Frame is a carbon fiber truss-like support structure. The Cold

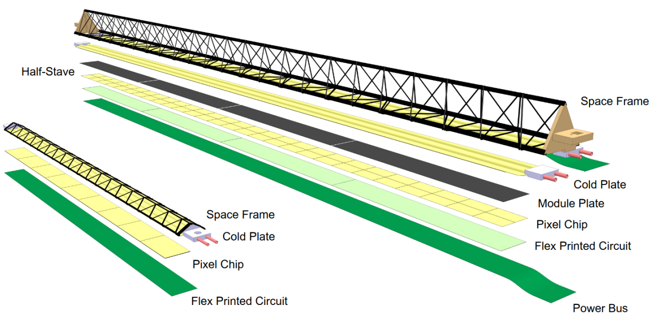

Figure 1.5: The ALICE IB and OB Staves with their respective components [14, p. 9].

Plate is a carbon ply containing cooling pipes. The Hybrid IC is a polyimide flexible printed circuit (FPC) hosting a 2×7 grid of Pixel Chips and some passive components. The Half-Stave is a component of the OB, hosting modules glued to a cooling unit. The material budget of ITS2 is very light, with a radiation length of 0.35 %X_0 per layer in the IB, compared to the previous ITS, which had 1.14 %X_0 per layer [19]. However, as light as ITS2 is, as seen in fig. 1.6's plot, only about 15% of this budget is from the silicon detectors (yellow at the bottom of the plot). In comparison, 50% comes from the FPC, 20% is attributed to the cooling circuit, and 15% comes from the supporting material[15]. This figure shows the periodic peaks of double the baseline at 0° and 30°. These peaks come from overlapping staves necessary to cover the azimuth, shown in fig. 1.7 as carbon, Kapton, silicon, aluminum, and glue, strongly raising the mean to 0.35%X/X_0. The blue peaks are from the water coolant corresponding to the two pipes/stave. If the supporting structures could be eliminated and only the silicon detectors remained, the material budget would be reduced by a factor of seven to 0.05%X_0 per layer. This is what ITS3 aims to achieve [20].

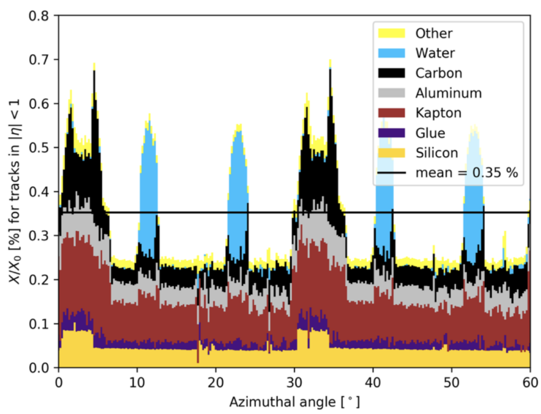

Figure 1.6: ITS2 Inner Barrel Material Budget taken from [15], peaks seen correspond to stave overlap shown in fig. 1.7.

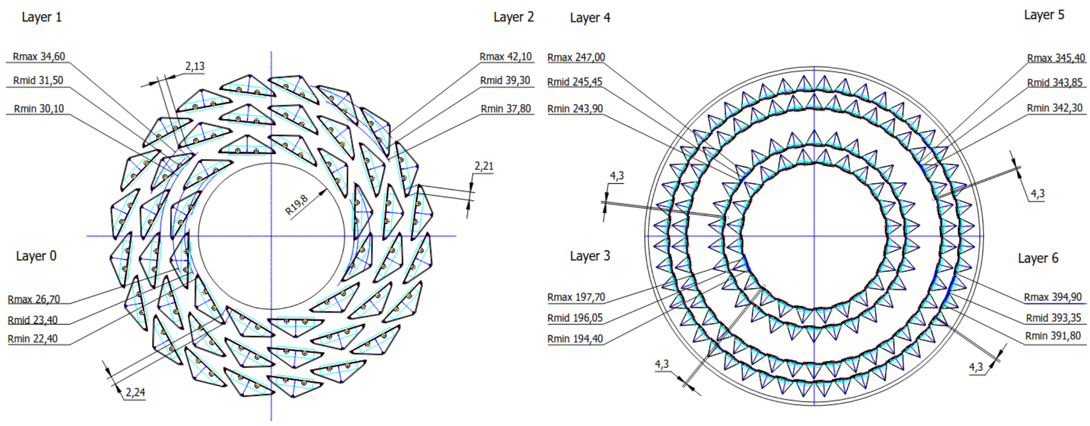

Figure 1.7: ITS2 Stave Cross Section, Showing IB Overlap Region from[14, p. 8].

1.3 ALPIDE Chip Properties

The ITS2 uses seven concentric layers of Monolithic Active Pixel Sensors (MAPS) composed of 0.18 µm Complimentary Metal Oxide Semiconductors (CMOS) [14]. MAPS combines a silicon diode and readout within the same pixel [21]. The key advantages of MAPS over hybrid pixel detectors are the low fabrication cost, they can be thinned down to reduce the material budget (or bend in for ITS3), they have individual pixel readout, they are fairly radiation hard, operate at high speeds, have a low power consumption from a single low voltage power supply [21, 22, p. 3]. The CMOS logic gates use p- and n-doped field effect transistors for logic functions. CMOS consumes very little power and produces minimal heat, which is ideal for reducing the material budget by reducing cooling needs and thermal noise. The MAPS track charged particles and have a spatial resolution of about 5 µm [20]. These MAPS are composed of a 512×1024 px matrix to form the ALICE Pixel Detector (ALPIDE).

The ALPIDE chip, was designed for the ALICE ITS2 upgrade that took place during the Long Shutdown 2 (LS2)[23] from 2019-2021[24]. The chip is 15 mm $\times$ 280 mm with and is put together as shown in fig. 1.8. The pixel pitch of ALPIDE measures 29.24 µm $\times$ 26.88 µm, upgraded from the original larger50 µm $\times$ 425 µm original ITS[19, 23, 24]. Each pixel contains a sensing diode, a front-end amplifier and shaper, a discriminator, and a digital component[25]. The digital component has three hit storage registers (Multi Event Buffer), a pixel masking register, and a pulsing logic [24]. This means that when a hit (a hit is when the charge collected in the charge collector is above the set threshold in the discriminator) is registered, the pixel's address is encoded in the signal propagated so that the coordinates of the hit are known. Signals are only propagated from pixels that register a hit (called 0 suppression). The front-end peaking time takes 2 µs and the discriminator pulse takes 10 µs.[24][25]).

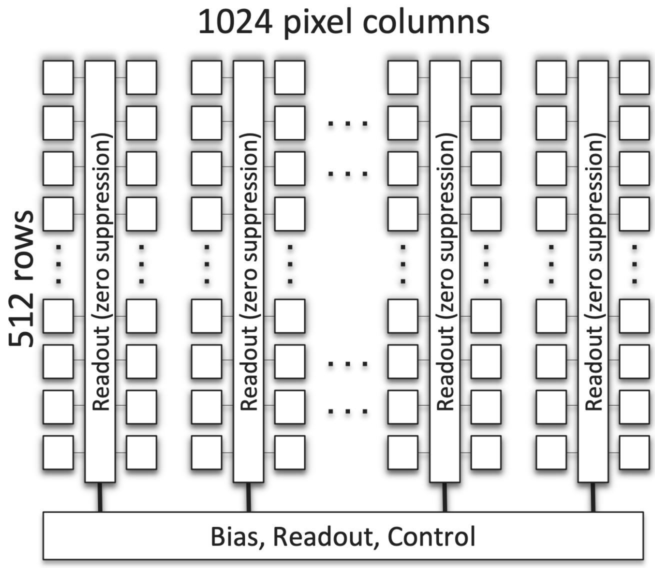

Figure 1.8: General ALPIDE Circuit Layout[24]

1.4 ITS3 Upgrade

The ALICE ITS will be upgraded again during the next long shutdown (LS3, scheduled from 2026 to 2028). While ITS2 is already an ultra-light structure with excellent tracking specs, there is still room for improvement. Most of the material budget comes from the support structure rather than the active part that is critical for the physics. As was already mentioned in fig. 1.6, only about 15% of the material budget comes from silicon. The increased size of the sensors using stitching has made it possible to exploit the flexible material properties of ultra-thin silicon so that a cylindrically bent self (mostly) supporting detector can be constructed. The elimination of the support structure and readout will reduce the material budget by a factor of seven.

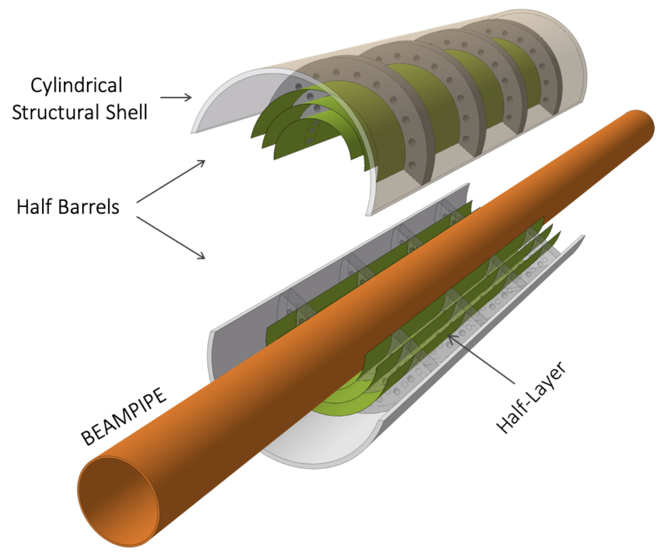

Figure 1.9: Diagram of planned ITS3 bent MAPS wrapped around beam pipe taken from [15].

The ITS3 upgrade will employ wafer-scale bent MAPS chips (shown in fig. 1.9). One of the main goals of ITS3 is to reduce the material budget. This will be achieved by removing the FPC (flexible printed circuit) and space frame, and the cooling will use air instead of water such that only silicon detectors remain. At ≈ 50 µm, silicon becomes flexible [20]. If the sensor becomes flexible, one no longer needs to use multiple sensors around the beam pipe but can bend two half-cylinder sensors around it, reducing the material budget since less support is necessary. This bent configuration will be held in place by carbon foam ribs[20]. Only the inner three layers are planned to be upgraded because they are the most critical. This configuration is also much simpler in the sense that rather than 432 flat sensors, there will be six cylindrically bent sensors.

The improved resolution of ITS3 should help the detection of low p_T particles ($p_T <$ 1 GeV/c), such as heavy flavor hadrons (charm and bottom), as well as low mass dielectrons.[15, 20]

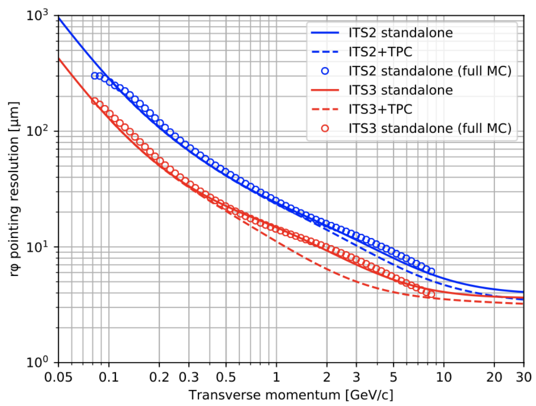

Figure 1.10: Impact parameter resolution and tracking efficiency from [15, 20]

The detector will be capable of facing a Pb-Pb collision rate of up to 100 kHz[15] (just as in ITS2[26]) and at least 400 kHz in p-p[14].

ITS3 will have to tolerate a 70% higher radiation load due to e^-e^+ pairs impinging on the ITS3 Inner Barrel which is closer than the ITS2 counterpart[15].

The innermost layer will be even closer to the interaction point, at 18 mm[20, 15]; the current radius is 23 mm following the 39 mm original ITS inner radius[23, 19, 27].

As mentioned, the major goal of ITS3 is the reduced material budget. This is accomplished by making one large wafer-scale monolithic detector. Chips are mass-produced on an industrial scale, and the application for the ITS3 upgrade demands, contrary to usual production, one large chip. The grid of many separate tiny chips carved from one wafer produced one large MAPS using a technique known as stitching. Stitching connects multiple small chips within the same wafer such that it forms one large monolithic circuit, which can be bent around the beam pipe.

2 Experimental Setup

This chapter details the test beam setup and the experiments carried out at the Cyclotron Center Bronowice, the kinematics of the test beam, and the first steps taken to unpack the raw data recorded.

2.1 Test Beam

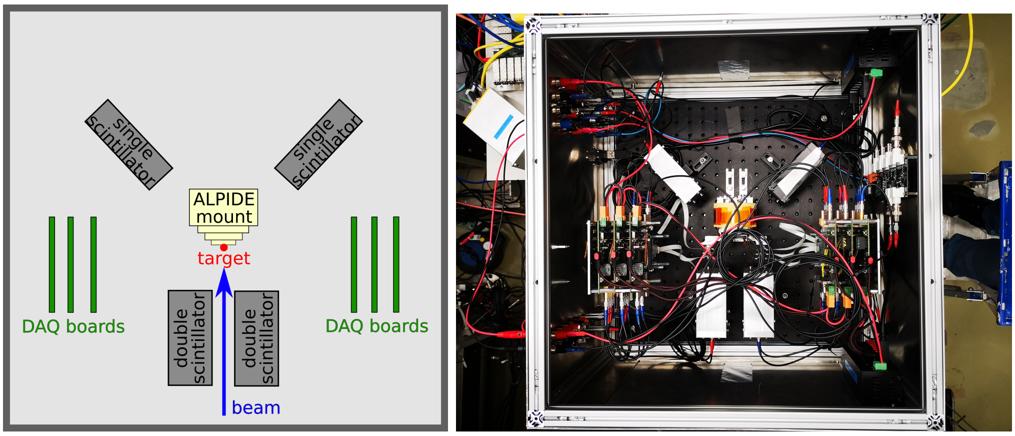

(a) μITS3 test beam setup (b) Setup in Dark Box

Figure 2.1: Experimental apparatus schematic and setup

On the weekends of November 1-15, 2022, experiments were conducted at the medical center and scientific facility Cyclotron Center Bronowice in Krakow, Poland (IFJ Institute). The cyclotron accelerated proton beams with a beam diameter of 4 mmFWHM to energies of 80 MeV, 120 MeV, 200 MeV that impinged upon a polypropylene $(C_3H_6)_n$ fiber target. The average momentum of the elastically scattered protons from this experiment is 278 MeV/c, 342 MeV/c, and 446 MeV/c, similar to the heavy flavor, low-p_T particles to be detected at the ALICE experiment by this detector. The beam spot can be seen in fig. 2.3. The target consisted of eleven fibers in an arrangement that resembled an arrow pointing toward the beam, as shown in fig. 2.2. The experimental setup can be seen in the photos fig. 2.4 and schematic fig. 2.1a. In addition to the μITS3 setup, other detectors used the test beam. This included CsI scintillators (CALIFA) and the silicon calorimeter SKIROC chips.

The aim of the μITS3 experiment was to learn how bent MAPS detect clusters and to explore different procedures for aligning trackers in the bent configuration. The fiber target was chosen because the collision between the beam and the hydrogen

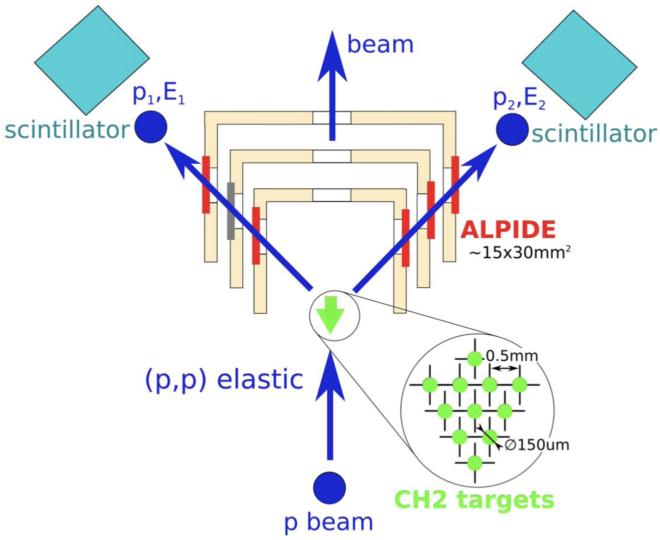

Figure 2.2: Fiber target with respect to experimental detectors and test beam

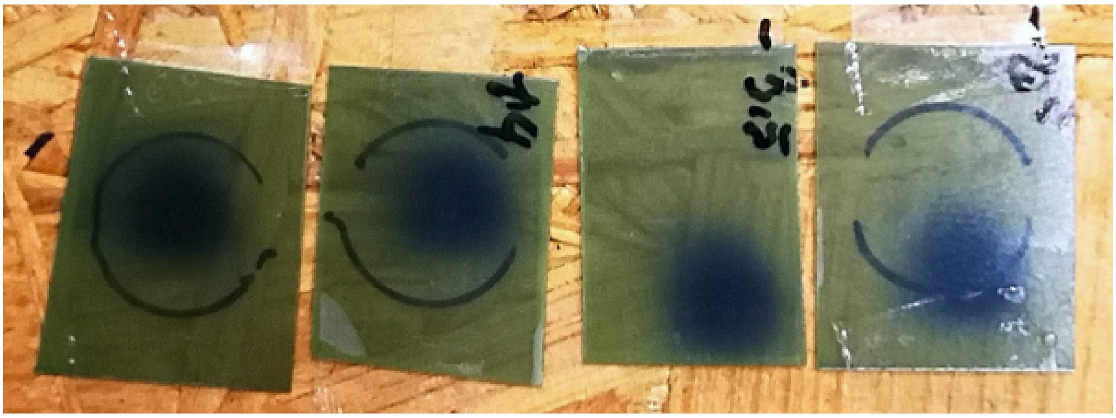

Figure 2.3: Photo of beam spot on radiochromic Film

in the target resulted in elastic scattering at a fixed opening angle, given the beam energy. The four-momentum is conserved in the scattering such that if one has the four-momentum of one proton, the four-momentum of the other proton in the collision could be reconstructed, and the other track could be retraced. In the telescope setup prepared at the CERN ITS3 Detector Lab, six ALPIDEs were bent around three cylinders of the ITS3 radius (18 mm, 24 mm, and 30 mm) with windows for the detectors, known as the μITS3 detector assembly was used at the test beam to qualify the vertexing abilities of the sensors at low momenta of 34.6 MeV/c, 52.6 MeV/c, and 86.7 MeV/c, from $E = \sqrt{p^2c^2 + m_0^2c^4}$ for proton energies 40 MeV, 60 MeV, and 100 MeV.

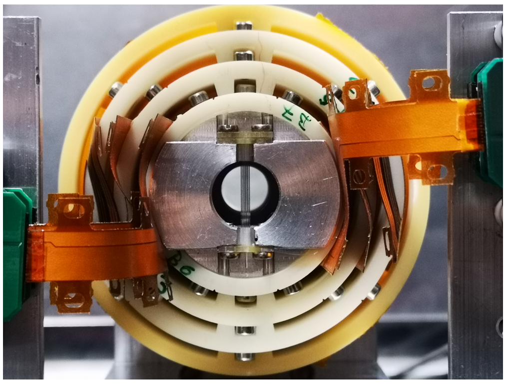

(a) Fiber Target Arrangement within ALPIDE Cylinders μITS3 setup as seen from Beam

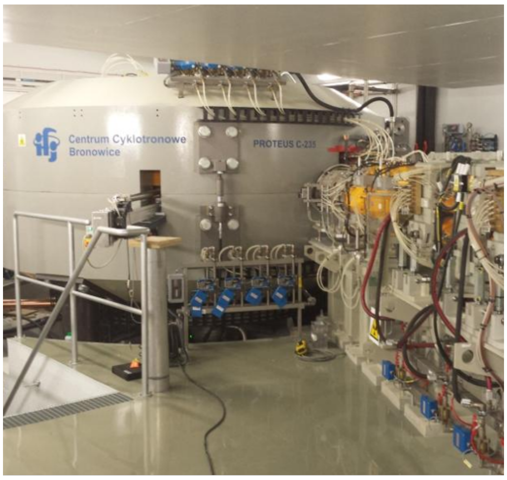

(b) IFJ's Proteus C-235 Cyclotron

Figure 2.4: Photos of experimental setup

2.2 Kinematics

In this section, the opening angle of elastically scattering particles will be solved from conservation of energy and momentum for particles of the same mass in the non-relativistic case to get a basic understanding. The relativistic effects are later taken into account using a simulation and are compared with experimental results. Quasi-free scattering between protons and a ^{12}C target was also simulated and compared with experimental results.

To calculate the opening angle elastic scattering between a projectile and target of the same mass, one begins with the conservation of momentum and energy. From conservation of momentum and energy:

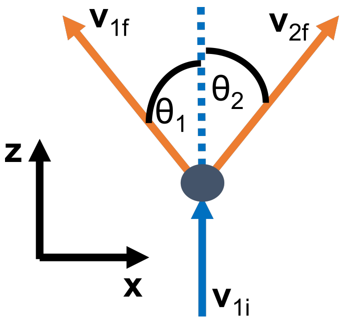

Figure 2.5: 2D Kinematics

$$m_1\mathbf{v}_{1i} + m_2\mathbf{v}_{2i} = m_1\mathbf{v}_{1f} + m_2\mathbf{v}_{2f} \tag{2.1}$$

$$\frac{1}{2}m_1 v_{1i}^2 + \frac{1}{2}m_2 v_{2i}^2 = \frac{1}{2}m_1 v_{1f}^2 + \frac{1}{2}m_2 v_{2f}^2 \tag{2.2}$$

Since the target proton is initially at rest, $\mathbf{v}_{2i} = 0$, and both protons have zero lateral momentum initially, $v_{1ix} = v_{1iy} = v_{2ix} = v_{2iy} = 0$ and $|\mathbf{v_{1i}}| = v_{1iz} = v_{1i}$. The particles all have the same mass, so that term drops out.

$$0 = v_{1fx} + v_{2fx} \tag{2.3}$$
$$0 = v_{1fy} + v_{2fy} \tag{2.4}$$
$$v_{1iz} = v_{1fz} + v_{2fz} \tag{2.5}$$

Due to the conservation of momentum, the scattering out of the beam axis must lie on the same plane. Since the coordinate system can be chosen arbitrarily, we simplify the equations by choosing the x-axis to go in-plane with the scattering. In this case, the y-momentum of both particles remains zero, so only eq. (2.3) and eq. (2.5) are left. To solve for the opening angle, one can take the dot product of the conservation of momentum equation with itself and compare it with conservation of energy, resulting in:

$$v_{1fx} = v_{1f}\cos(\theta_1), \quad v_{1fy} = v_{1f}\sin(\theta_1) \tag{2.6}$$
$$v_{2fx} = v_{2f}\cos(\theta_2), \quad v_{2fy} = v_{2f}\sin(\theta_2) \tag{2.7}$$
$$\begin{aligned} v_{1i}^2 =& v_{1f}^2[\sin^2(\theta_1) + \cos^2(\theta_1)] + v_{2f}^2[\sin^2(\theta_2) + \cos^2(\theta_2)] \\ &+ 2v_{1f}v_{2f}\cos(\theta_1)\cos(\theta_2) + 2v_{1f}v_{2f}\sin(\theta_2)\sin(\theta_2) \end{aligned} \tag{2.8}$$

Using trigonomic relations:

$$v_{1i}^2 = v_{1f}^2 + v_{2f}^2 + v_{1f}v_{2f}\cos(\theta_1 - \theta_2) \tag{2.9}$$

And finally, inserting the conservation of energy $v_{1i}^2 = v_{1f}^2 + v_{2f}^2$, the particles' angular relationship to the z-axis comes out:

$$\cos(\theta_1 - \theta_2) = 0 \tag{2.10}$$

This forces a fixed opening angle of $\theta_1 + \theta_2 = 90°$, which allows the particles freedom to lean more to the left or to the right depending on how the z-component of momentum is distributed. This is illustrated in fig. 2.5. This result is valid for the non-relativistic case only. In the 80 MeV to 200 MeV, the opening decreases up to only 3° due to length contraction in the laboratory reference frame. The opening angle has a width, as seen in the plot fig. 2.7, because of how the "wobble" unequally shared momentum among protons along the beam axis. Since the protons have four different momenta, the length contraction varies and results in a broadened opening angle distribution.

2.2.1 Proton-Proton Elastic Scattering

The opening angle was determined in advance so that the position of the chips could be determined in advance to correctly be able to see the full track (schematics illustrated in fig. 2.8). The opening angle is fixed and depends on the beam energy and reaction as shown in the table 2.1. From the conservation of momentum, the sum of momentum orthogonal to the beam must remain zero, but the momentum along the beam axis does not have to be shared equally. This can be at any azimuth to the beam, but the angle between the protons remains fixed.

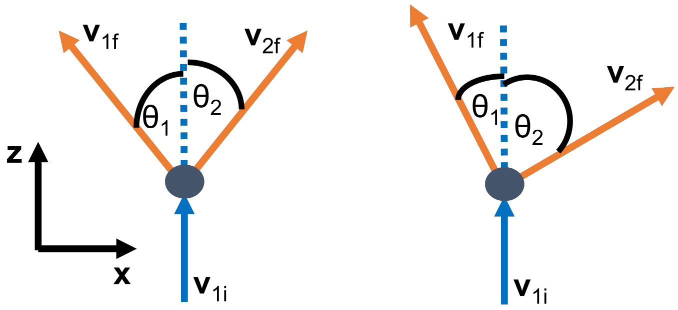

Figure 2.6: Illustration of freedom of scattered particles to unevenly distribute momentum along the beam axis.

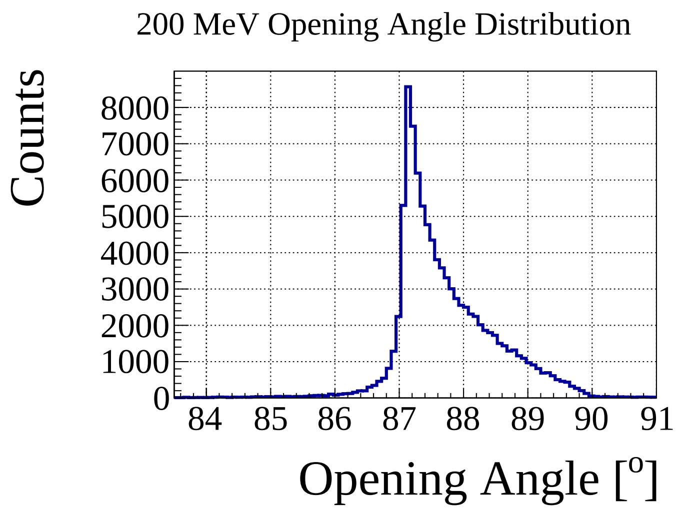

Figure 2.7: Simulation of 200 MeV beam p-p elastic scattering opening angle (simulation developed by [28]).

2.2.2 Quasi-Free Scattering

During the second weekend, the setup was moved to observe the expected opening angle of quasi-free scattered protons. At first, it was anticipated that a second peak from the scattering of ^{12}C would be visible because of the carbon in polypropylene $(C_3H_6)_n$). Inelastic scattering scattering with carbon occurs by the knockout reaction channel: p(^{12}C, ^{11}B) 2 p. The average opening angle $(\theta_1 + \theta_2)$ can be calculated from the binding energy by the formula eq. (2.11):

$$cos(\theta_1 + \theta_2) = \frac{E_b}{2E_1} \tag{2.11}$$

where E_b is the binding energy of the knocked-out nucleon, and E_1 is the energy of the incident proton (beam energy) [29]. From this formula, the average opening angle was calculated with results for different beam energies in table 2.1. Later, when the experimental opening angle results were plotted, no peak from found ^{12}C quasi-free-scattering was observed. Quasi-free nucleon-nucleon scattering (proton knockout) in

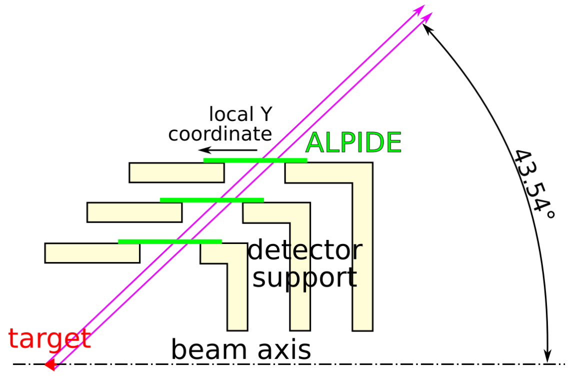

Figure 2.8: Choice of position of detectors with respect to the target was chosen in advance according to the opening angle.

Table 2.1: Elastic and Quasi-Free Opening Angles at Different Energies

Beam Energy [MeV]	**200**	**120**	**80**
p-p Elastic Scattering Opening Angle	87.08°	88.20°	88.76°
p-p Quasi-Free Scattering Opening Angle	82.56°	79.82°	74.78°

the direct kinematics reaction p(^{12}C, ^{11}B) 2 p did not produce a sharp peak due to the strong dependence on the intrinsic momentum of the nucleon knocked out[30]. The internal momentum of nucleons in ^{12}C causes a broadening of the expected opening angle. Sometimes, the intrinsic momentum goes with the impinging proton; other times, it goes against the beam. After boosts, this leads to a very broad distribution of opening angles, as opposed to the sharp peak observed from the p-p elastic scattering since the free proton in the target has no intrinsic momentum. In the simulation shown in fig. 2.9, the expected distribution of opening angles was performed and appears in good agreement with the experimental results, which can be viewed in chapter 8.

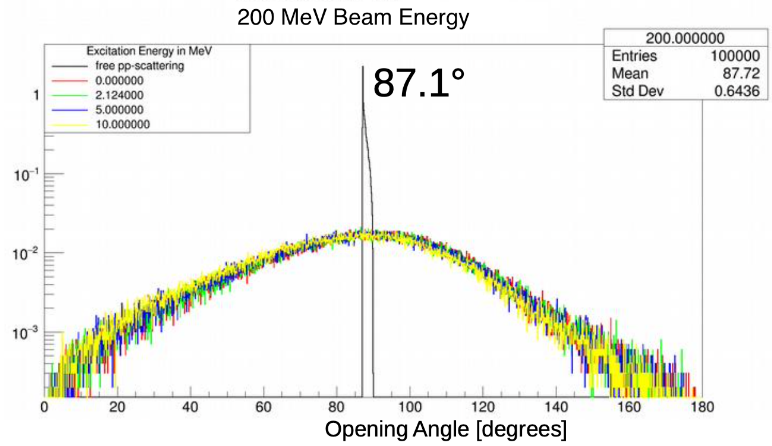

Figure 2.9: Simulated distribution of opening angles at 200 MeV test beam energy, including quasi-free scattering and elastic scattering reaction channels. [provided by T. Jenegger]

2.3 Energy Correlation with CALIFA

CALIFA (CALorimeter for In-Flight detection of gamma-rays and high energy charged pArticles), was used to measure the energies of protons coming from the target measured during the beam time. The anti-correlation between arms can be seen in fig. 2.10. The energy of protons from the same event sum up to the beam energy minus energy loss inside the μITS3 material as expected from the elastic p-p kinematics.

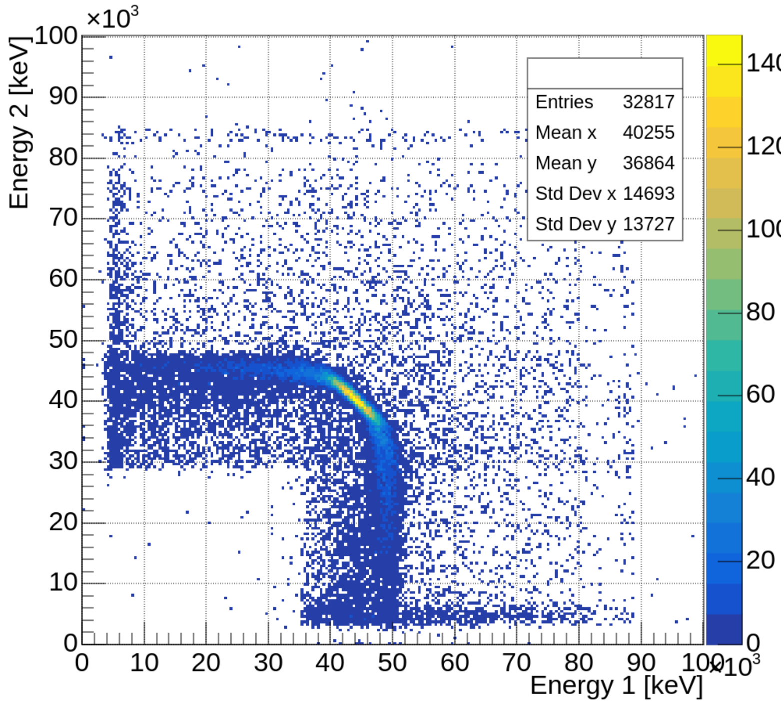

Figure 2.10: Energy correlation plots from CsI scintillators for events from the test beam [data processed by T. Jennegger]

2.4 Data Analysis

The data was analyzed using Corryvreckan, Python, and ROOT to correlate hits on the detectors, to separate noise, background, and signal, to reconstruct tracks, and to align the detectors. A hit has a nanosecond timestamp, charge information, and the row and column of the pixel that fired. A cluster is a collection of neighboring pixels in space that registered hits within a time window. The cluster size is the number of pixels.[31] The software developed in this analysis is accessible under this GitHub repository.

2.4.1 Corryvreckan

In the first stage of data analysis, the Corryvreckan ([32, p. 1]) test beam analysis software (developed in collaboration with CERN) was used to plot events detected by the ALPIDE's online. In addition, it can convert data from the raw data files into ready-for-analysis root and pickle (.pkl) files while cutting out noisy pixels. The Corryvreckan framework also built clusters from single-pixel.

In the earliest stage of analysis, hit maps were plotted, and the target could be indirectly observed using the EUDAQ2 event loader. The hit map of particles upon each ALPIDE can be seen in fig. 2.11. As expected, the particles scattered off the target at the right angle directly onto the ALPIDEs, as is seen as a square in the middle of each detector.

In Corryvreckan, the geometry of the detectors was configured, where the relative positions and rotations of all detector layers with their respective bending radii were defined. With this, it was possible to obtain the positions of measured clusters in global lab coordinates instead of the local coordinates on the chip as initially measured by each ALPIDE.

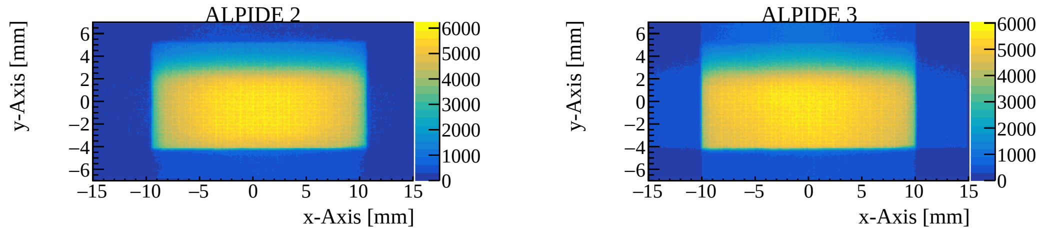

(a) Hit Map of Inner Layer Detectors

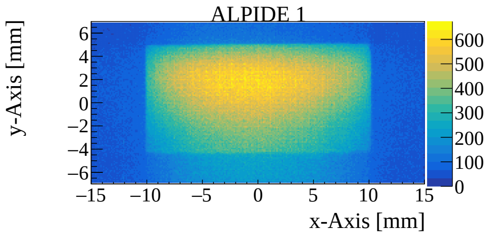

(b) Hit Map of Middle Layer Detector

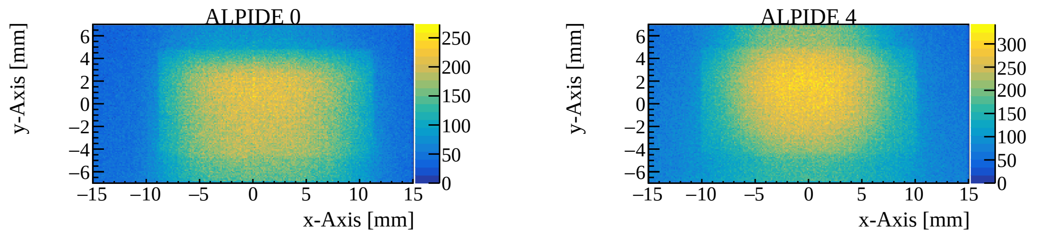

(c) Hit Map of Outer Layer Detectors

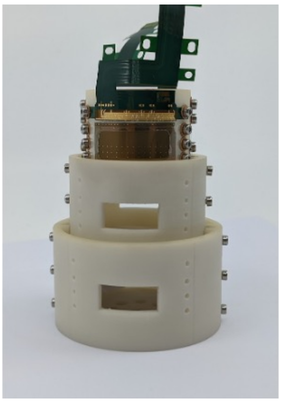

(d) "Window frame" ALPIDE is strapped to can be seen as the rectangular border causes multiple scattering reactions with protons incident

Figure 2.11: Hit Maps for Detector Layers on Left and Right Arms with rectangular shadow visible from the plastic structure holding the ALPIDEs

2.4.2 Geometry

The geometry of the ALPIDEs within the Corryvreckan framework was verified to ensure the coordinates of hits were correct and ready for analysis. Corryvreckan has preset geometry for ALPIDEs that may readily be applied. In the case of the experiment carried out, bent Cartesian coordinates were used. The geometry was visualized using the RootInteractive [33] python library, which uses Bokeh [34] for plotting and can be seen in fig. 2.12.

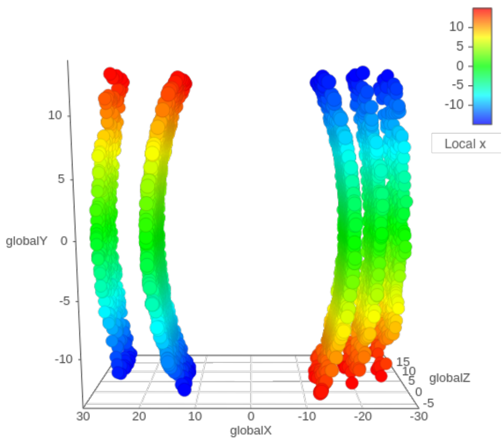

Figure 2.12: ALPIDE's "local" detector coordinates compared with global laboratory rectilinear coordinates as obtained from measured clusters. Here is local x.

The step of transforming local coordinates to global coordinates is very important to form tracks so that clusters on an ALPIDE may be plotted with a common origin. In order to perform such a transformation, one must recall that the local x of our system corresponds to the azimuth about the beam axis and that the local y corresponds to the position along the beam axis (albeit anti-parallel). The radius is presumed to be fixed for each cylinder due to the very precise bending of the ALPIDE chips. As a reminder, the inner barrel detectors ALPIDE 2 and 3 had a radius of 18 mm, and the middle barrel detector ALPIDE 1 had a radius of 24 mm. The outer barrel detectors ALPIDE 0 and 4 shared a radius of 30 mm. In order to go from local coordinates to global coordinates, we then have all of the information necessary. Clusters were detected in the local detector coordinate system and extracted using the Corryvreckan framework, which assigned global coordinates to clusters in addition. Using the following equations, clusters are transformed into the laboratory frame.

$$\begin{aligned} x_{\text{global}} &= R\cos\left(\frac{x_{\text{local}}}{R}\right) \\ y_{\text{global}} &= -R\sin\left(\frac{x_{\text{local}}}{R}\right) \\ z_{\text{global}} &= -y_{\text{local}} - 7.5\,\text{mm} \end{aligned} \tag{2.12}$$

2.4.3 Clustering

The neighboring hits registered on detectors in the same event time frame were clustered into *cluster* objects by Corryvreckan. To analyze data outside of the event loader framework, Corryvreckan was used to convert the .raw files to .txt and combine neighboring hits into clusters with properties including the number of pixels, local detector coordinates, and charge, saved as part of an event with any hits detected synchronously on the other ALPIDEs. All clusters on each ALPIDE at the time of

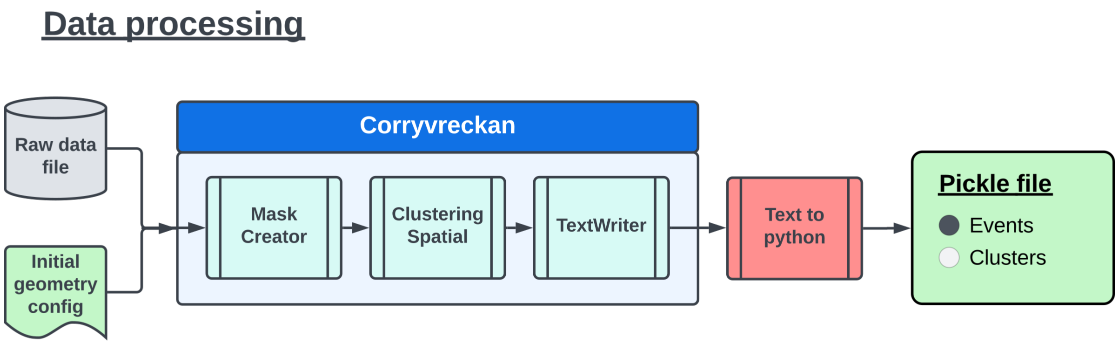

Figure 2.13: Flow chart of data processing

an event are saved to the event. A convenient feature of Corryvreckan was that it automatically eliminated hot pixels by cutting out pixels that fire more than fifty times more compared to the average pixel.

The cluster information was converted into custom-developed event classes defined in Python and saved to .pkl files for storage, as illustrated in fig. 2.13.

2.5 Tracking

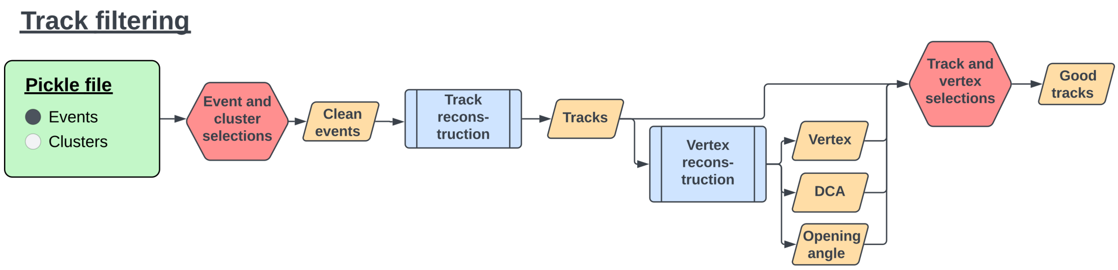

Figure 2.14: Tracking procedure

In this section, the procedure of reconstructing tracks from clusters is discussed. Since no external field was applied, tracks were assumed to be straight and were constructed by fitting a line to the measured clusters on each arm, as illustrated in fig. 2.15. Since it is desirable to have clean events, and there is ample data, events that had exactly one cluster on each (functioning) detector were selected. This simplifies the tracking procedure because it means two separate tracks through the same detector in the same event did not have

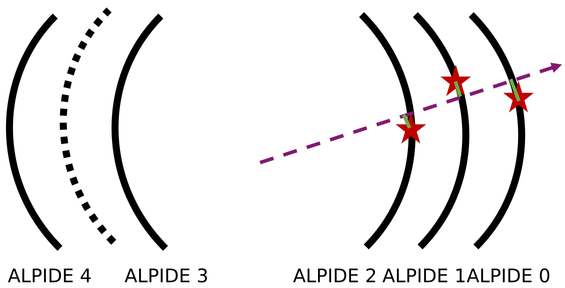

Figure 2.15: Since no magnetic field was applied, tracks were constructed using a linear fit of the hits on each arm. In the case of the left arm, this is simply a line between the two functioning detectors

to be sorted out from each other. On the other end of the extreme, events that did not have less than one cluster on each arm were not used because either there would not be enough points to form a track or a track could be formed but would not be desirable because it does not carry information about the quality of the track in the arm. To quantify the quality of the track, the RMS of the distances between the clusters and the constructed line was used.

2.5.1 Vertex Reconstruction

The vertex was reconstructed using the point of closest approach between the two tracks. The reconstructed vertex is defined as the midpoint of the shortest possible line that can be drawn between two tracks. This can be visualized from the illustration in fig. 2.16. The reconstructed vertex is shown in fig. 2.17, which is distinctly recognizable as the target from the test beam (a 3D version of the vertex and its clusters points, plotted next to an illustration of the experimental setup is shown in fig. 2.18). The ring around the bottom XY perspective of the vertex is the aluminum sample holder. The gradient of vertex points emanating from the center-right side of the target as seen from the XY perspective is the beam spot. The DCA distribution is very broad, which is from the misalignment of the detectors, and from the lack of cuts applied on this data. Alignment will be discussed in detail in chapter 4, which is dedicated to investigating different alignment strategies to eliminate the blur of the detectors and by minimizing the DCA of tracks.

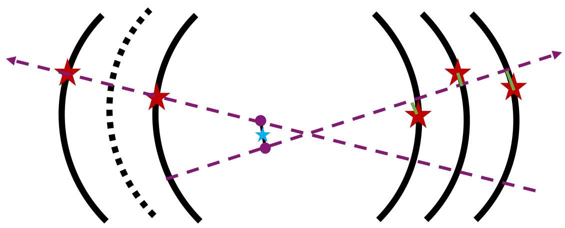

Figure 2.16: The vertex point is calculated as the midpoint of the shortest line that can be drawn in between the two tracks

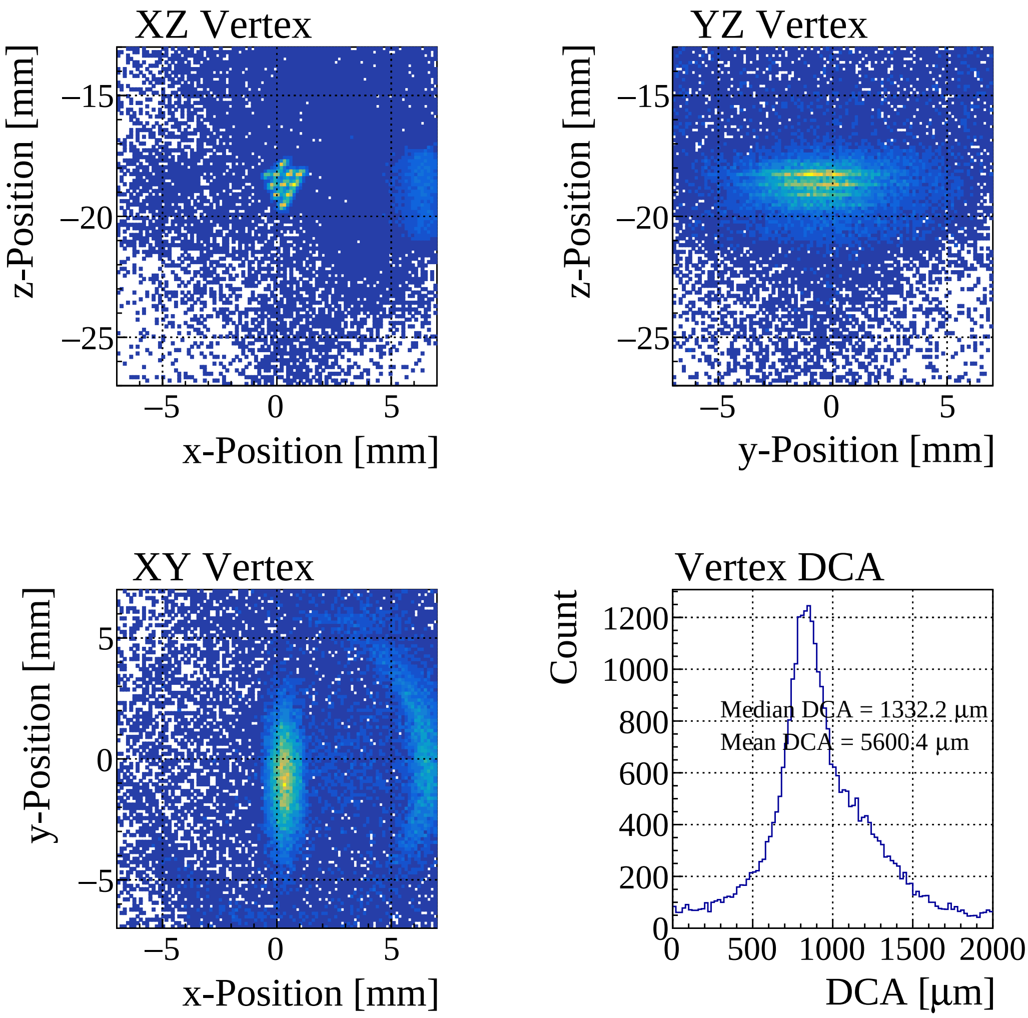

Figure 2.17: Reconstructed vertex from raw data before alignment, as seen from top (XZ), side (YZ), and front (beam perspective, XY) and DCA distribution.

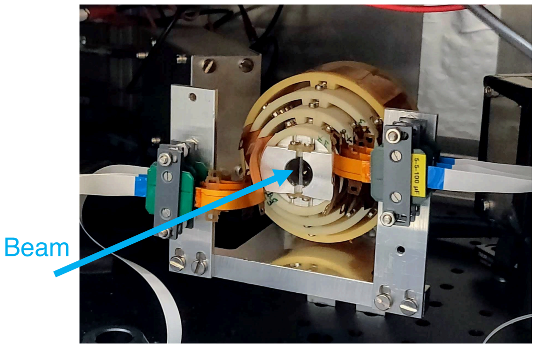

(a) Experimental Setup Photo

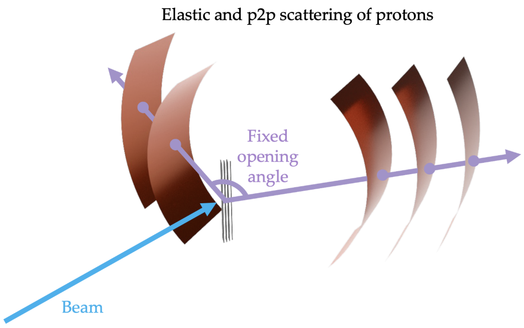

(b) Experimental Setup

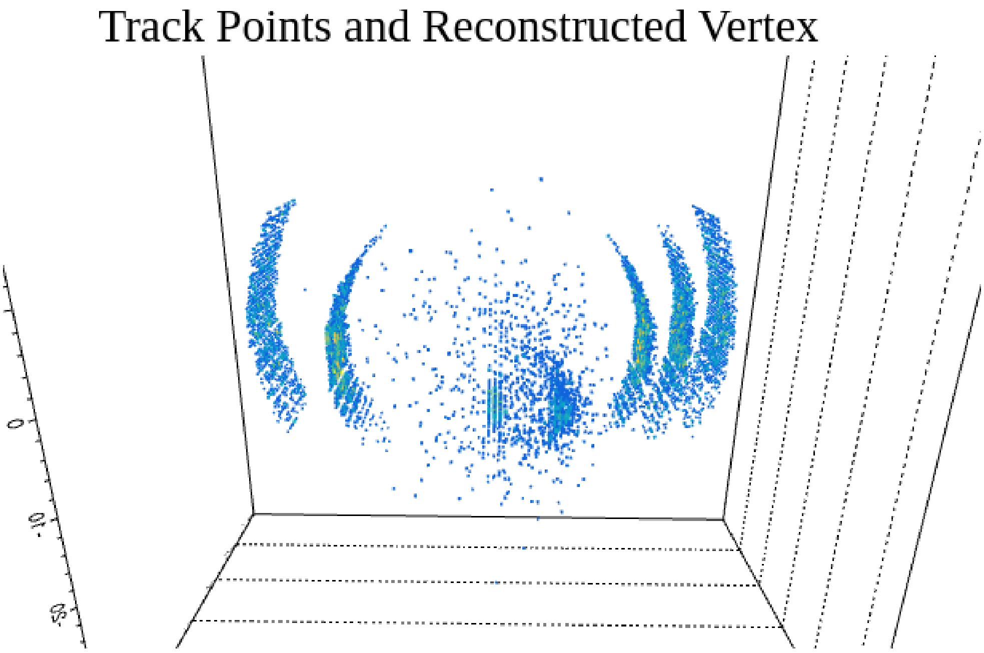

(c) 3D plot of reconstructed vertex and clusters that form its tracks

Figure 2.18: 3D Vertex reconstruction with illustration of experimental setup

3 Cluster Analysis

In this chapter, a comprehensive analysis of the measured clusters will be described in detail. First, the different cluster sizes seen in a plot without any cuts applied will be explained, discussing the type of particle detected and the source of it. Next, the analysis of the effect of different charge collection thresholds on cluster sizes for all beam energies is examined. Following the charge collection threshold analysis, the chapter will be closed by discussing cluster size dependence on the angle through the detector.

3.1 Cluster Size Data for PID

Before applying any cuts on the cluster data, the cluster size distribution at 200 MeV for all detectors looks like fig. 3.1. One peak is immediately visible for all detectors centered around 15 pixels but spanning 5 to 25 px corresponding to protons, and a background contribution for smaller cluster sizes is around 3 pixels. The former corresponds to δ-electrons, secondary ionizing electrons ejected from matter in the path of the primary beam. These particles left much smaller cluster sizes due to their low energy loss compared to the protons, which are in the highly ionizing momentum range. Most of the detected δ's were absorbed by the innermost detectors facing the beam, shielding the outer layers. This can be observed from the high small-sized-cluster occupancy of ALPIDEs 2 and 3 compared to the outermost layer detectors ALPIDEs 0 and 4 in fig. 3.1, and the overall higher cluster occupancy for outer layers in fig. 3.2. With this distinction, deltas were filtered out of the data later in the analysis by cutting out smaller clusters.

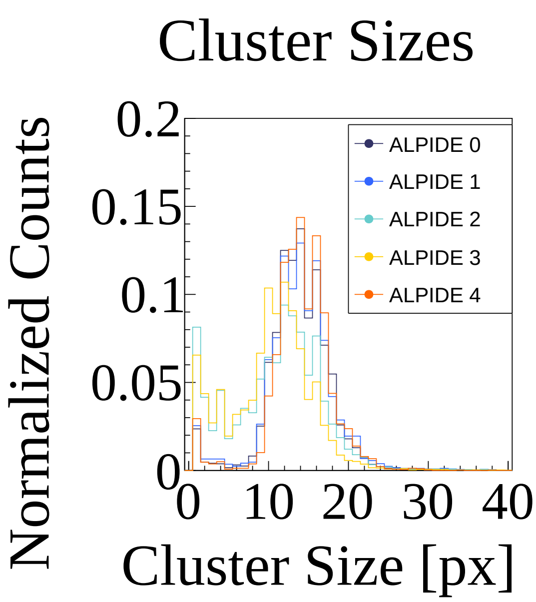

Figure 3.1: Cluster sizes at 200 MeV and 100e threshold, distribution on all detectors normalized to total cluster counts.

The latter, more prominent peak centered about 12-15 px are mainly from the protons scattered off the fiber target but also has a contribution from the aluminum sample holder, which has a broad distribution that will be discussed in section 3.1.2. Indeed, the reconstructed vertices not only included the fiber target but also included collisions from the beam with the aluminum target holder, air, the plastic mount of the detector, the detector itself, and delta electrons generated by the beam. Therefore, it is useful to make geometric cuts on certain regions to compare the cluster size distributions. The selection of clusters from a region is made by cutting on the vertex formed by the cluster's track. As mentioned in chapter 1, the tracked clusters are limited to clusters from events in which exactly one cluster was measured on each detector to select for clean events.

3.1.1 Target Region vs. Background Region

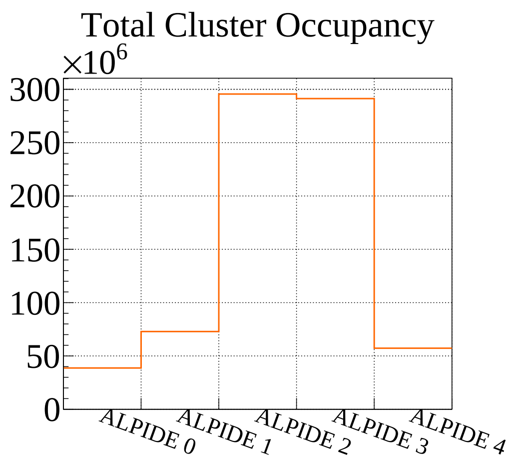

Figure 3.2: ALPIDE Cluster Occupancy at 200 MeV beam energy and 100e charge collection threshold.

Before comparing the cluster size spectrum from different regions, another step is necessary. One must normalize with respect to the volume so that the density of different-sized clusters can be compared. This is achieved using the global coordinate system (in mm) defined by eq. (2.12). The target region volume is restricted to:

$$x \in [-2, 2]$$
$$y \in [-5, 5]$$
$$z \in [-20, -17]$$

The background volume is bounded by the following:

$$x \in [-4.5, 4.5]$$
$$y \in [-6, 6]$$
$$z \in [-23, -15]$$

Excluding the target region contained. These boundaries are illustrated by the red boxes surrounding the target region in fig. 3.3. This cleaned data significantly reduces the first peak caused by delta electrons, as seen in fig. 3.4. The small cluster size's relatively large occupation of δ-electrons are much smaller even in the background plots of this figure when compared with fig. 3.1 because the normalization to volume makes it look smaller compared to normalization with the area under the plot. δ-electrons still make up a $\sim 5\%$ share of the clusters. The more significant percentage of deltas in the non-target region is more important to notice. This is very useful because it means if the cluster size density distribution in the non-target area is subtracted from the target

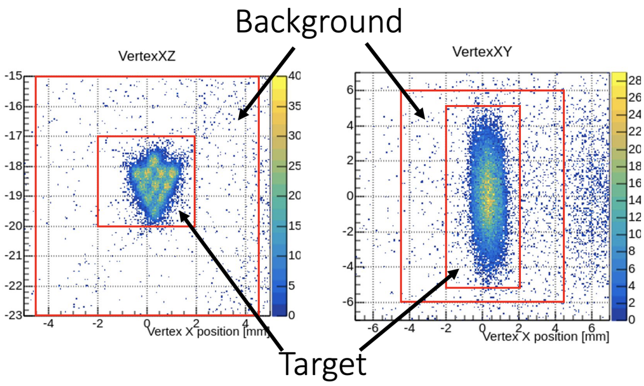

Figure 3.3: Target and Non-Target Vertex Region Normalizations

region, the background will be removed from the fiber target.

Once again, it can be seen that not only the inner detectors but also the middle detector (ALPIDE 1) carry a larger share of small clusters (<5 px) compared to the outer sensors. ALPIDE 3 has a larger shifted cluster size distribution due to an error that rendered a higher charge collection threshold. From fig. 3.4a, one can see that, as expected, most of the clusters come from the target region, but the distribution of clusters from other sources can be cut out.

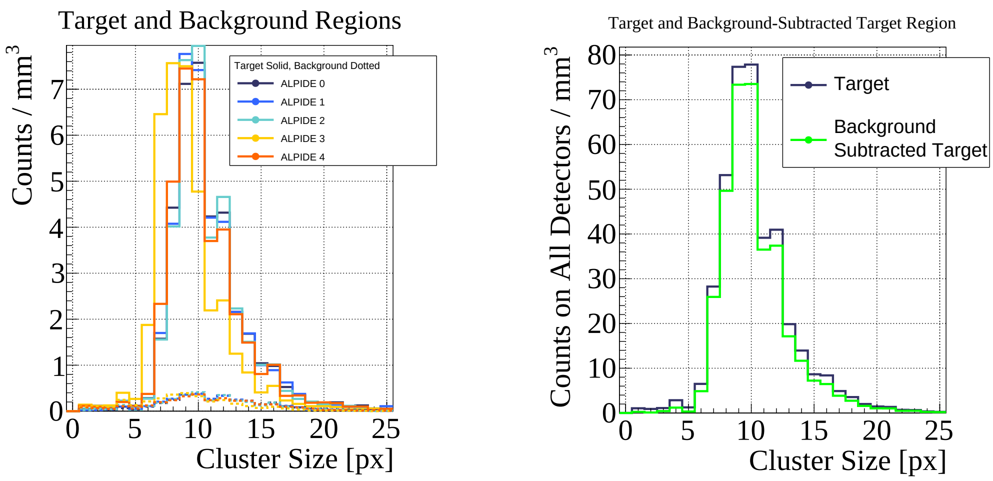

(a) Cluster sizes in target vs. background.

(b) Cluster sizes in target region before and after the background was subtracted

Figure 3.4: Cluster size distribution before and after the background has been removed at 200 MeV and 100e charge collection threshold.

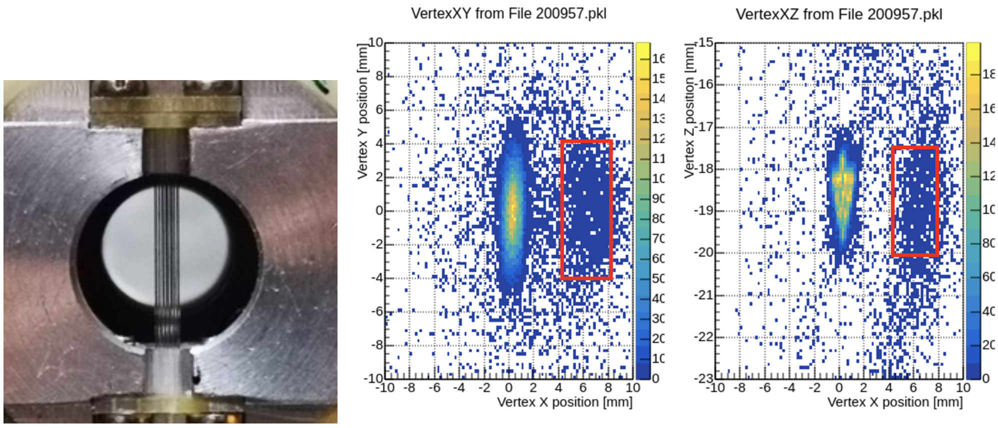

(a) Aluminum target holder

(b) Selected Aluminum Region

Figure 3.5: Aluminum sample holder volume where aluminum clusters were selected from.

3.1.2 Aluminium Target Holder

In addition to the fiber target, the beam scattered off of the aluminum sample (seen in fig. 3.5) holder and was detected. Obviously, the beam spot was not perfectly centered, and a small fraction of the particles hit the target holder on the right-hand side, as shown by the gradient of reconstructed vertex points towards that side of the plot. The homogenous background is due to reactions in the air. This background was subtracted (shown in fig. 3.4b) from the data to isolate the fiber target signal the experiment aimed to observe. Fortunately, selecting both sides of the distribution fig. 3.6b shows the distribution of cluster sizes over the observed region at different beam energies on the left and right sides of the beam axis. The number of entries from the right side of the reconstructed vertex ($x > 0$) is populated by more clusters overall than the left ($x < 0$) side. More importantly, though, the shape of the cluster size distribution demonstrates that the aluminum sample holder contributes by providing a broader distribution of particles with lower momentum on the right side of the vertex compared with the left.

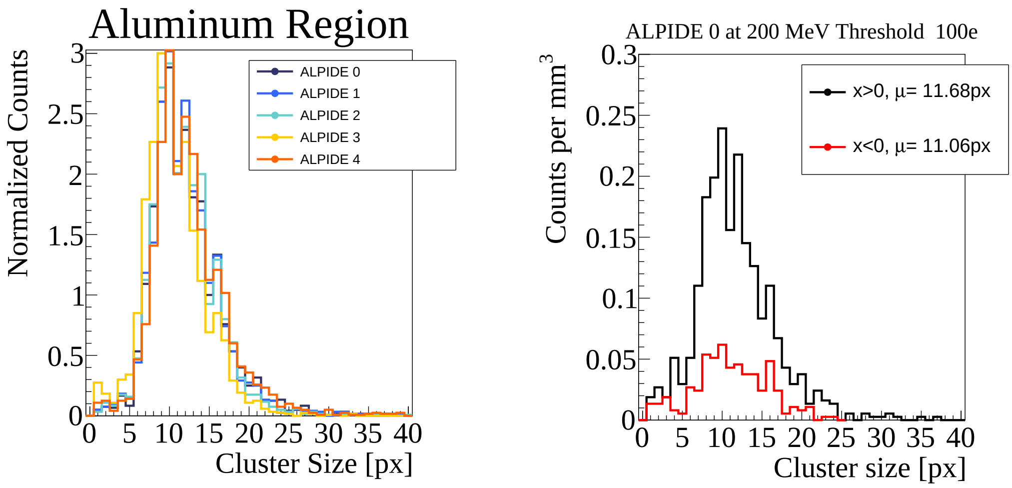

(a) Clusters from selected aluminum region (from 200 MeV beam and 100e threshold)

(b) Left vs. right background regions from 200 MeV beam and 100e charge collection threshold.

Figure 3.6: Comparison of cluster sizes in aluminum regions and left and right side of background region

3.2 Electron Collection Threshold

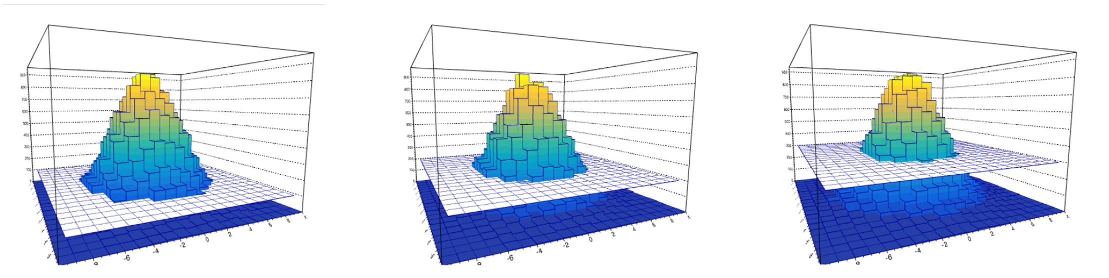

Figure 3.7: The 100e$^-$, 200e$^-$, and 300e$^-$ threshold planes against a Gaussian distribution representing pixel occupancy and e$^-$ counts

Before discussing the electron charge collection threshold, it is important to understand how clusters form at different beam energies. Since cluster size is nothing more than the number of adjacent pixels in the detector that reached the charge collection threshold during an event, the size depends on the number of electrons liberated in a region. The number of free electrons is determined by the energy deposited in the epitaxial layer of silicon, which can be calculated using the relativistic Bethe formula eq. (Bethe 1932 [35]).

$$-\frac{dT}{dx} = \frac{2\pi N Z z^2}{m_e v^2}\left[\ln \frac{2 m_e v^2 W \gamma^2}{\bar{E}^2} - \beta^2\right] \qquad \text{Bethe 1932 [35]}$$

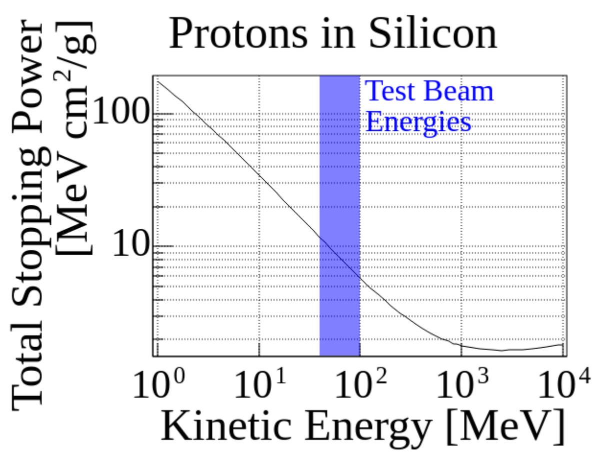

Figure 3.8: Bethe-Bloch Curve Through Silicon from [36]. using the relativistic Bethe formula eq. (Bethe 1932 [35])

where T is the kinetic energy of the projectile, x is the path through the stopping medium, $\bar{E}$ is the average atomic excitation energy of the target, z is the projectile's charge (in our case, it is the proton's charge 1), and Z is the target's atomic number (for silicon, it is 14). N is the number density of target atoms. W is the maximum energy transferred in a collision. β and γ are the normal relativistic factors, m_e is the rest mass of the electron. This was plotted for silicon using data from [36] in fig. 3.8. The light blue-shaded region highlights the energy of protons scattered from the target. Here, it can be seen that the energy deposited in silicon decreases with beam energy at the test beam energies. This indicates that the cluster size should decrease at higher beam energies, which is what is observed. The electron charge threshold is the amount that has to be collected for the pixel to send a readout signal. Increasing the charge threshold effectively cuts down the number of pixels sending signals in a region, thereby shrinking the cluster size, as illustrated in fig. 3.7. The charge collection threshold of

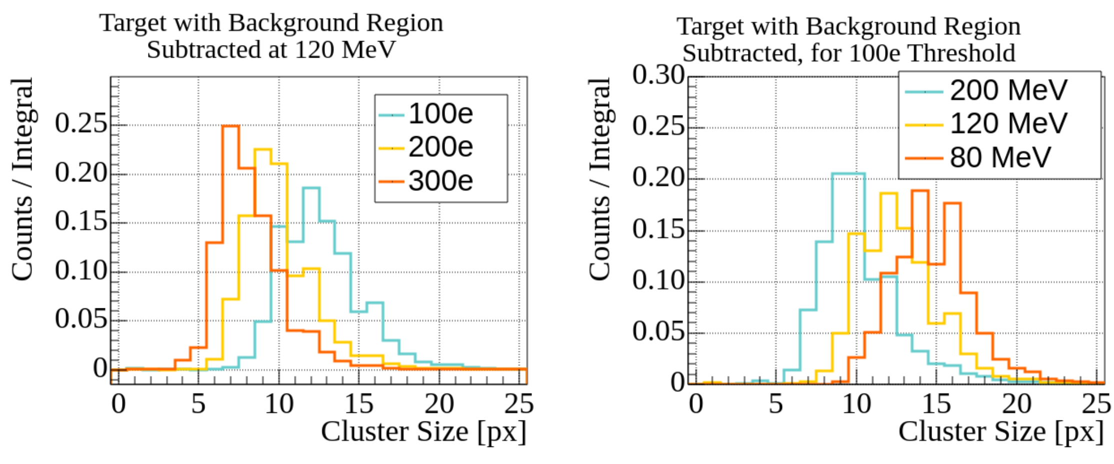

(a) Clusters from normalized background region at all charge collection thresholds (120 MeV beam)

(b) Distribution of cluster sizes for different beam energy settings and a pixel threshold of 100 e−

Figure 3.9: Comparison of charge collection thresholds and beam energies on cluster size distributions.

the ALPIDEs behaved as anticipated. As shown in fig. 3.9a, the cluster sizes decrease with the electron threshold (the minimum charge required to trigger the pixel is larger; hence, fewer pixels are triggered, and the cluster size is smaller). Hence, the charge collection threshold can be used to tune the detector's sensitivity. The side of the Bethe-Bloch curve the proton energies were on was such that higher energy protons interacted less with the detector, which generated less charge as seen in **??**. This can also be seen in the aforementioned figure, where a monotonic decrease with beam energy is given a fixed threshold. This information is summarized in **??**.

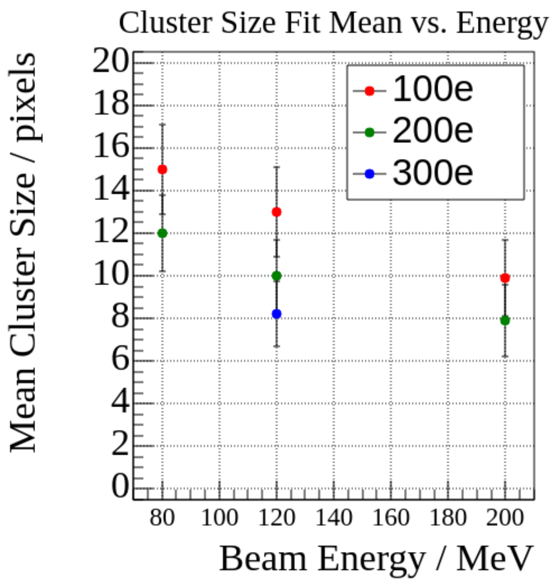

Figure 3.10: This plot summarises the threshold and beam energy effects on the cluster size. As would be expected, the cluster size increases with energy deposited in the detector and with lower electron collection thresholds

3.3 Cluster Sizes For Tracks at Different Angles Through Detectors

Table 3.1: Cluster sizes vs. energy deposited in an ALPIDE, (assuming a 45° impact)

Mean Proton Energy [MeV]	Energy Loss in ALPIDE [keV]*	Mean Cluster Size [px]
40	134.84	15.1
60	98.23	13.3
100	67.07	9.9

The path length through the detector did not strongly correlate with cluster size as shown in fig. 3.11a, which is at first surprising because there is more detector volume for charge to be generated in. Upon closer inspection, it is realized that the same region

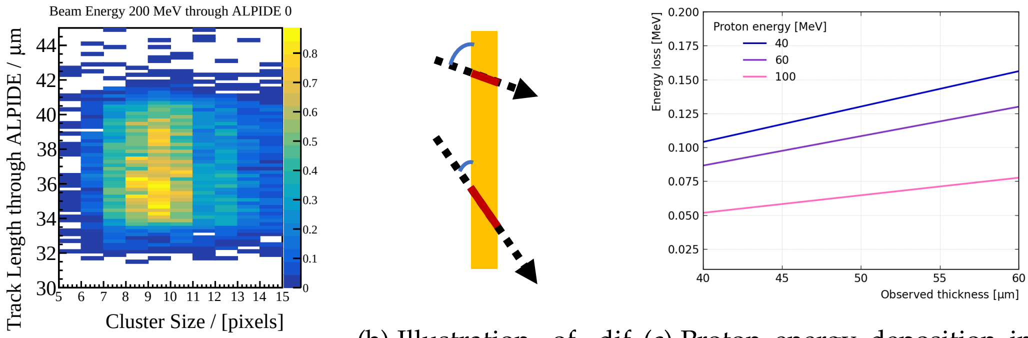

(a) Effect of path length through detector on cluster size at 200 MeV and 100e threshold.

(b) Illustration of different path lengths through detector depending on the angle of incidence.

(c) Proton energy deposition in silicon as a function of path length plotted using the Bethe-Bloch formula for protons of half the test beam energies.

Figure 3.11: Cluster size sensitivity to track length through detector volume.

that is populated by tracks passing through more material, is also populated by higher momentum protons, as the higher momentum protons will have smaller angles from the beam axis, as explained in chapter 2. Higher momentum protons deposit less energy in the detector volume due to the side of the Bethe-Bloch curve they lie on, as is seen by the lower energy loss for the higher energy protons plotted in fig. 3.11c. These two competing effects might explain why it is hard to see a correlation between the cluster size and the path length through the detector.

4 Alignment

To accurately reconstruct particle paths within detectors, precise knowledge of detector positions is essential for track reconstruction. Traditionally, alignment corrections focus on the locations where detectors are attached and can move. Detectors are typically adjusted using rectilinear coordinates due to their flat geometries and alignment along the rectilinear axis. While second-order effects, like the angle of the mount, are considered, they usually play a minor role due to the constraints imposed by the detector's rigid structure.

However, the introduction of bent geometry alters the alignment considerations. The mounting is no longer flat, introducing the angle of the mount as a degree of freedom (DOF). This means detectors can now have angular displacements relative to each other, a freedom not present in previous geometries. The cylindrical geometry, with shared barrel mounts, implies that if one barrel is misaligned, the misalignment will be reflected in all attached detectors.

Additionally, the introduction of bending to the thin chip introduces new challenges. The bent chip, as seen in the case of μITS, is secured using multiple screws, allowing for variations in fixing from one edge to the other. This introduces more degrees of freedom, thereby increasing the complexity of the correction process and potentially creating more points of failure that need correction.

The alignment was carried out by changing the local x and y coordinates because they were positioned in failure points of the alignment already. After the initial trial of alignment using the local coordinates, global coordinates were employed to allow for rotations about the vertical access of the barrel, as the assembly of the μITS barrels were attached and could be at an angle of O(0.1°), expected to have a minor effect compared with the azimuth, which could rotate more discretely.

The alignments were applied to all detectors separately by modifying the coordinates of all clusters in the detector being shifted by a given shift. Next, the event tracks were formed (using single cluster events as detailed in chapter 2) on the shifted system, and then the distance of the closest approach (DCA) between the tracks was compared. Since the two tracks come from a single point (where the initial beam particle struck the target), assuming the particles do not interact between the target and the detectors, the two tracks should be traced back to that same point. However, this ideal scenario is limited due to multiple scattering reactions of the protons. The interaction of the particles with the detectors themselves, the target fibers, and the air all result in multiple scattering. The cross-section and scattering angles are small, so the effect is not very large but still imposes a lower bound on how small the DCA can be.

4.1 Simulation of Tracks

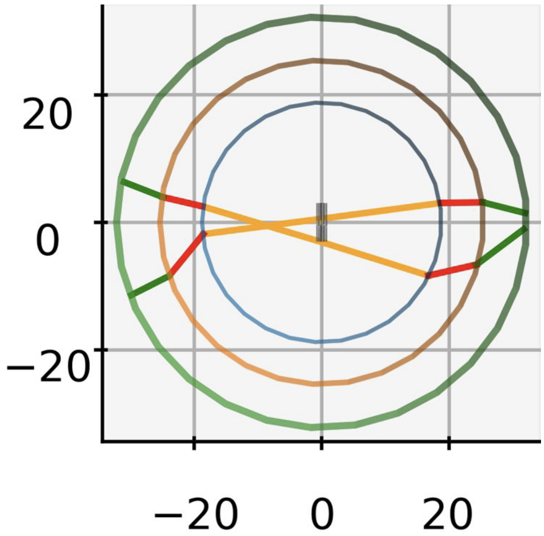

(a) Simulated Multiple Scattering of Two Events (exaggerated scattering angles by a factor of 1000 for visualization)

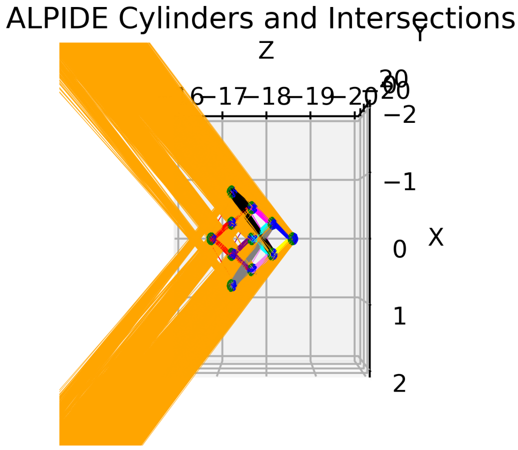

(b) Simulated multiple scattering between fibers with full statistics and real scattering angle. The colors of the track represent which fiber the track passed through or the intersection with the detector in the case of orange tracks.

Figure 4.1: Simulated multiple scattering figures drawing tracks

A track simulation was crucial to anticipate the expected outcomes in an optimally aligned scenario. Establishing an objective for alignment procedures, was important to qualify the alignments against an ideal model. Critical investigations, such as the blur of target fibers, the optimal achievable DCA considering multiple scattering effects, and the relative impact of scattering off target fibers compared to the detectors, were effectively addressed through the analysis of simulated tracks.

The smallest DCA was calculated as 11 µm in a perfectly aligned detector system scenario using simulation. This was the mean value, instead of the median, taken as there is no tail to cut off the simulated data. The simulated results are shown in fig. 4.2. The energy transferred to silicone with protons at the high energies used is low (for protons of kinetic energies 40 MeV, 60 MeV, and 100 MeV, the highest expected energy fraction transferred was 0.34%). The scattering angle for 100 MeV protons and radiation length can be seen in table 4.1. The scattering angles in table 4.1 were calculated using eq. (Highland 1975 [37]), where p is the proton's momentum and β is the ratio of the proton's velocity to c (in the 100 MeV proton case p =446.28 MeV/c and $\beta = 0.429529$). L is the distance traveled through the scattering medium, and L_R is the radiation length (mean distance through the material for an electron to travel and lose $1/e$ of its energy)

Material	Radiation Length (X_0)	Scattering Angle
Silicon	9.370 cm	1.08 mrad
Polypropylene	49.47 cm	0.617 mrad
Air at 1 atm	3.039×10^4 cm	0.406 mrad

Table 4.1: Scattering Angles for 100 MeV Protons and Radiation Length Values for Different Materials for Their Path Length in the Experiment (radiation length values taken from [38])

of the material.

$$\theta = \frac{14.1\,\mathrm{MeV}}{p\beta}\sqrt{\frac{L}{L_R}}\left(1+\frac{1}{9}\log_{10}\left(\frac{L}{L_R}\right)\right) \qquad \text{Highland 1975 [37]}$$

4.1.1 Distance of Closest Approach Lower Bound

The DCA lower bounds were calculated by randomly generating tracks from the fiber targets at the opening angle for the given beam energy with random azimuth. Each time the track intersected with a detector layer, a vector at a randomly chosen scattering angle from a Gaussian distribution about the scattering angle, with a random azimuth about the track, was added to the track from the intersection onward. If the line missed the detector, it was excluded from the data just like the single cluster event cuts made on the real experimental data. The simulated intersections with the detectors were then used to generate new tracks that fit the intersections, and then the DCA between the two tracks was calculated. This procedure is illustrated in fig. 4.1 using 50,000 events. The intersection with the simulated middle detector in the right arm, although it existed in the simulation and simulated multiple scattering, was not used to generate data for intersection points used in track reconstruction to match the broken detector in the experimental data.

Moving the detectors to select the smallest DCA should align the detector system. Additionally, one would expect the root mean squared distance (the average radius of cluster positions between tracks) to be minimal in an aligned system. Unfortunately, this could only be done for the right arm (because the right arm's middle detector was broken.

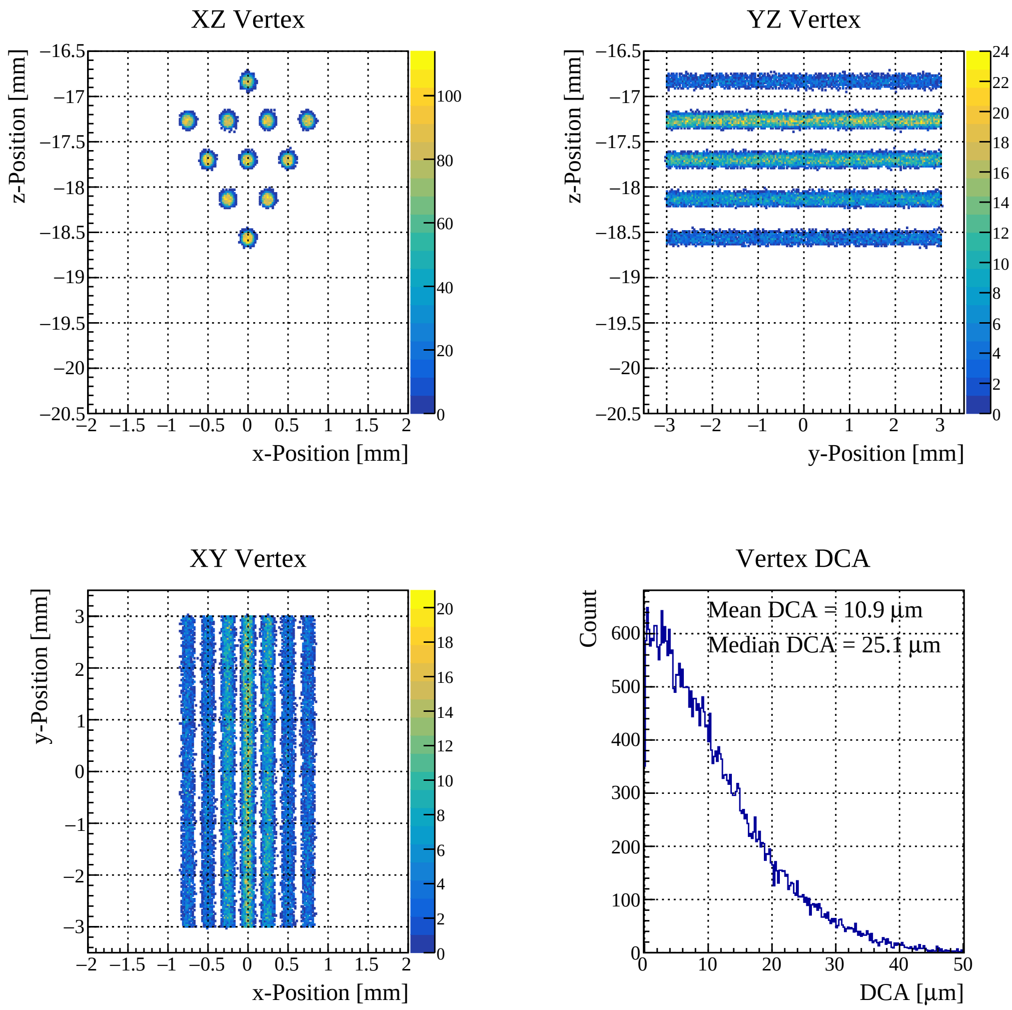

Figure 4.2: Vertex reconstruction including multiple scattering in the target and detector material.

4.2 Cuts Applied on Experimental Data

For alignment, it is of utmost importance that the tracks are from a clean sample of proton tracks with minimal background. Thanks to the ample data supply from the test beam, it is possible to apply very hard cuts, which would not be possible if the data set was small.

The data had to be selected carefully to simplify the analysis. As motivated by the investigation conducted in chapter 3, a cluster size cut between 7 px and 20 px was applied. The root mean square distance of the clusters in the right track to the tracks themselves was bounded by <2 mm. Cuts on the vertex were also made. The DCA of the tracks traced by the detectors should be near where the fiber target was expected to be, usually within less than 2 mm of the target. An additional constraint to selecting the protons from the fiber target was based on the opening angle of the outgoing particles, typically between 85° and 90°.

The events with reconstructed vertices lying near the expected target position are used to exclude particles striking from the aluminum housing of the target fibers. This was done by selecting the region that appeared to be the fibers when the reconstructed tracks formed a vertex region.

Since elastic proton-proton collisions were selected, the opening angle evaluated from the tracks was used to cut out events that did not resemble p-p collisions at a given beam energy.

Additional cuts were made to cut out the plastic region as shown in fig. 2.11d; the detectors were taped to limit tracks significantly affected by multiple scattering.

In fig. 4.3, one can see a reconstructed vertex without any alignment applied. One would expect the vertex to be sharper and not distorted as it is now if it were not for misalignment.

4.3 Alignment Strategies

One of the challenges of bent detectors is the novelty of aligning an angular geometry. Previously, the ITS was aligned using a flat geometry with mainly Cartesian degrees of freedom. The vertex and DCA distributions, as well as the coordinate shifts of all of the alignments described in this section which are not already plotted can be found in chapter 8.

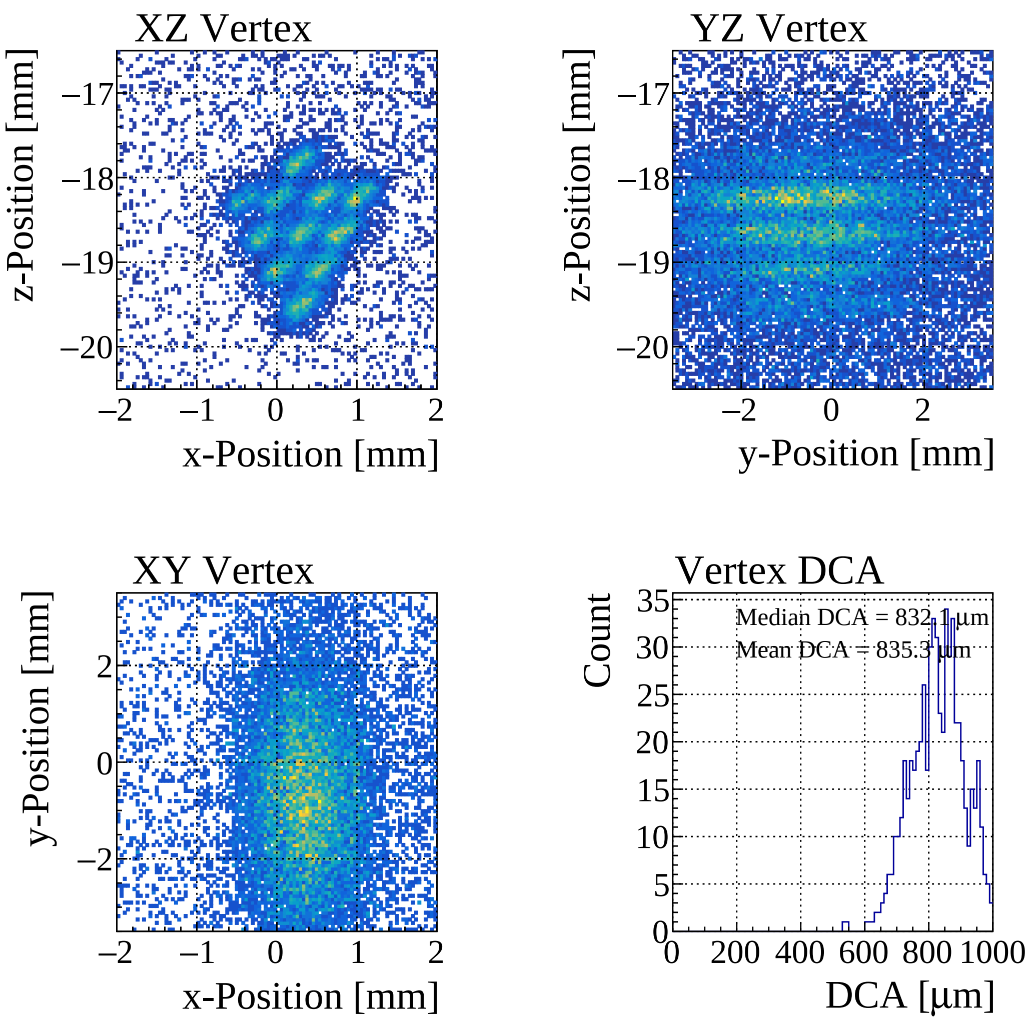

Figure 4.3: Reconstructed vertex without any alignment applied

4.3.1 Kinematic Constraint Alignment

Kinematic alignment works in the case of the setup used here, thanks to the convenient property of elastic scattering lying in the same plane. Conservation of momentum forces the momentum of the system to have zero momentum transverse to the beam since, initially, all the momentum was along the beam axis of the projectile proton. These collision planes can be drawn from any selection of ALPIDEs with at least one detector on each arm. The out-of-plane detectors' average displacement from the plane can then be calculated, corresponding to the beam axis's azimuth since it is orthogonal to any event plane formed due to the kinematic constraint. The broadness of the distribution corresponds to the displacement from the beam axis. In fig. 4.4, the displacement of detectors from all reaction planes can be seen. The detectors forming the plane are lines marking the zero while the remaining two detectors' positive or negative azimuthal displacement (in mm related by local-$x = r\phi$ as mentioned in chapter 2) is

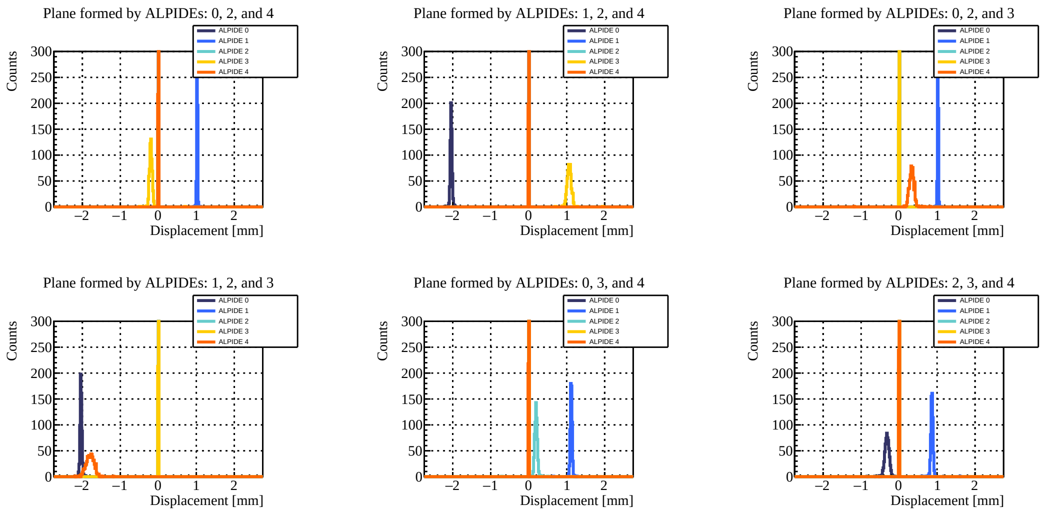

Figure 4.4: Displacement of measured clusters against event planes constructed from different groupings of ALPIDEs. The in-plane detectors are lines at zero for reference, the remaining two detectors form a two-dimensional distribution. Since the beam axis is mostly in the plane, the plot strongly correlates with the local x alignment and is mainly correlated with local y in the width of the distribution.

marked by their displacement from zero. The width of the distribution corresponds to other sources of misalignment or deviation from perfect elastic scattering (effects from multiple scattering could be to blame for example). The kinematic plane displacement results for the aligned scenario can be found in chapter 8.

4.3.2 Single Detector Bisection Alignment

A general alignment that does not depend on kinematic constraints is needed for the planned ITS3. Therefore, an approach was taken where an observable that depends on the alignment quality is minimized by exploring the possible geometric configurations. In the case of this algorithm, the DCA, which, if the alignment is perfected, should converge to the limit imposed by random multiple scatterings, was used. The algorithm developed here moves the individual detectors around and evaluates the DCA in search of better-performing configurations. The algorithm uses a bisection approach to avoid having to probe the entire space of possible detector positions. Through many iterations, the position of individual ALPIDEs within the laboratory was shifted along the detector coordinates (azimuthal rotation and translation along the beam axis). The following algorithm carried out the shift: given the local-x and local-y intervals and the number of iterations to be carried out as parameters, the median DCA was minimized. The median (as opposed to the mean) was chosen because a "tail" may partly originate from non-p-p elastic scattering events in the distribution that skews the mean value. In the first iteration, the algorithm would calculate the median DCA for the "corners" of the configuration (these being a rectangle formed by the outermost coordinates in the x

and y range). In the following iteration, a new rectangle is formed by the middle point of the corners from the last round, and the lowest median DCA configuration is found from those explored in the previous iteration. This effectively slices the space explored in half each round, zooming in on a region with the smallest median DCA value.

This algorithm relies on a two of assumptions:

- The minimal median DCA should be a reliable proxy measurement of alignment.
- The algorithm relies on the median DCAs in the configuration space being monotonic towards the global minimum median DCA, or else the configuration could converge on a local minimum. This approach should still converge to a global minimum regardless of starting configurations as the DCA is expected to be convexly correlated with the detector position.

This algorithm was carried out one detector at a time. After each detector was aligned, it was found that the whole system would get stuck in a local minimum and that a more promising approach would be to explore a wider range of configurations.

4.3.3 Multiple Detector Bisection Alignment

To explore a broader range of configurations, each detector was simultaneously shifted. This yielded much better results than the single detector alignment but with a much longer computing time. Shifting all five detectors simultaneously did not converge on an alignment. Instead, an anchor detector had to be chosen to converge on a configuration. In this particular case, eight dimensions are shifted to minimize the median DCA value. After setting the search range so that it would arrive near the ALPIDEs 1 and 2 to the values found using the kinematic constraint alignment, the configuration converged to the values shown in section 8.2 and section 8.2, where the vertex can be seen in fig. 4.5. The algorithm was parallelized by running one configuration on each core. In the case of the quad-core parallelization used, it took $\sim$2 hours to complete the ten-dimensional alignment and $\sim$45 minutes to complete the eight-dimensional alignment.

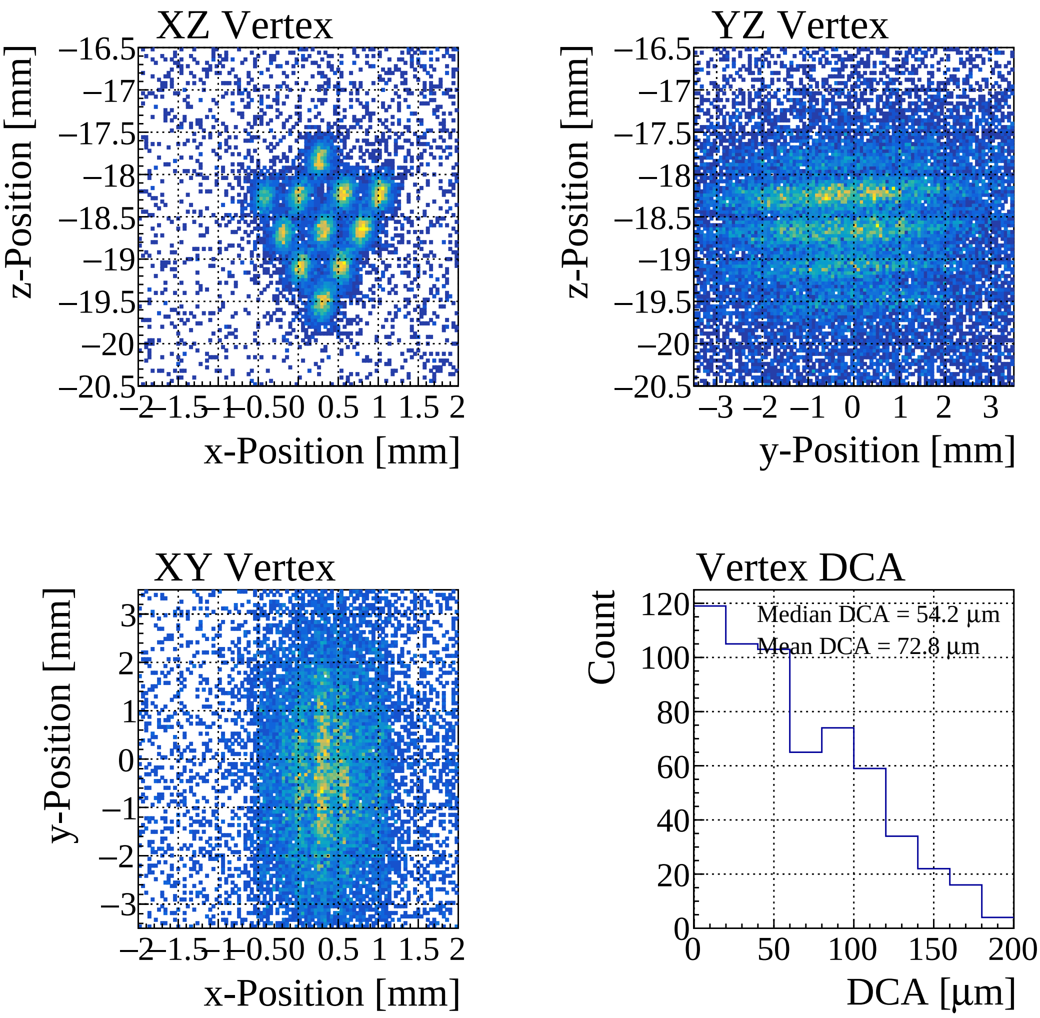

Figure 4.5: Reconstructed vertex using an eight-dimensional alignment strategy (ALPIDE 0 held fixed, with ALPIDE 1 and 2 starting ranges restricted to the neighborhood of kinematic constraint found shift values).

Barrel Twist

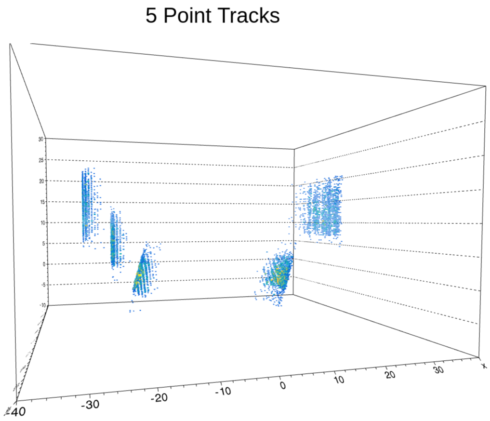

Figure 4.6: Left-Right Barrel Rotation Degree of Freedom

After having aligned the detectors along the beam axis, and about the azimuth, the next degree of freedom to be corrected was the twist of the barrel. This was accomplished by providing a third degree of freedom for each detector: a rotation about the chip's vertical (polar) axis. This rotation can be visualized by the twist of the inner barrel detectors in fig. 4.6. One would expect that the barrels could be misaligned by a left-right or top-bottom skewing of the barrel, so ALPIDEs on opposite sides of the same barrel should converge on the same angular displacement. This degree of freedom was applied both on top of the results from the bisection alignment and as a separate degree of freedom such that each detector had three degrees (along the beam axis, azimathally, and polar). Since in both cases, the angles found were almost zero (0.06°) at most, it was observed that this barrel twist was not observed in the setup, and the holding structure ensures the barrels are parallel.

5 Physics Performance

This chapter compares the alignment results at different energies, the change of the opening angle after alignment, and plots energy correlation recorded with CALIFA scintillator.

5.1 Alignment Results

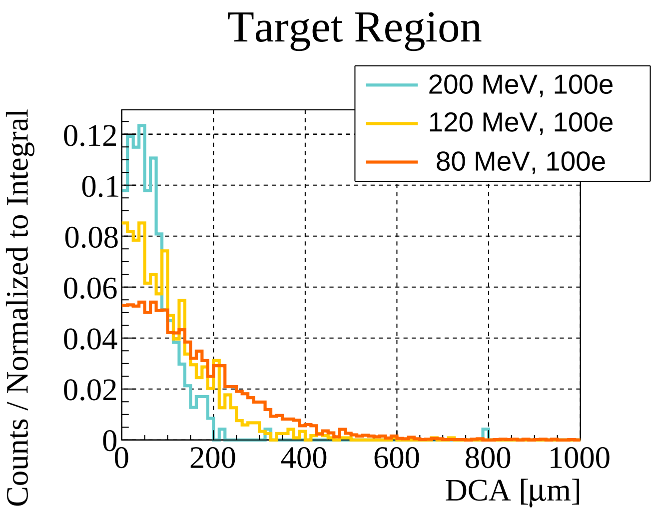

Figure 5.1: Vertex DCA for alignment applied to all tested beam energies

Using the highest quality alignment applied to the beam energies tested, a histogram of the distribution of DCAs was plotted in fig. 5.1. It can be seen that as the beam energies decrease, the width of the distribution increases. This is explained by the momentum's effect on the proton's scattering angle through matter. Momentum is inversely proportional to the scattering angle according to eq. (Highland 1975 [37]), used in the multiple scattering simulations. It seems very likely that the DCA limit of $\sim$55 µm is fundamentally due to multiple scattering. If the air were included in the scattering simulation, perhaps the mean DCA, too, would have been close to 50 µm.

5.2 Opening Angles Compared with Simulation

The opening angle plotted in chapter 2 was smaller than the expectation. It is assumed that this is at least partially due to the remaining misalignment of the detectors. In fig. 5.2, the opening angles did improve as the distributions for all three beam energies overlap better when applying the alignment from the eight-dimensional bisection approach, found in chapter 4 applied.

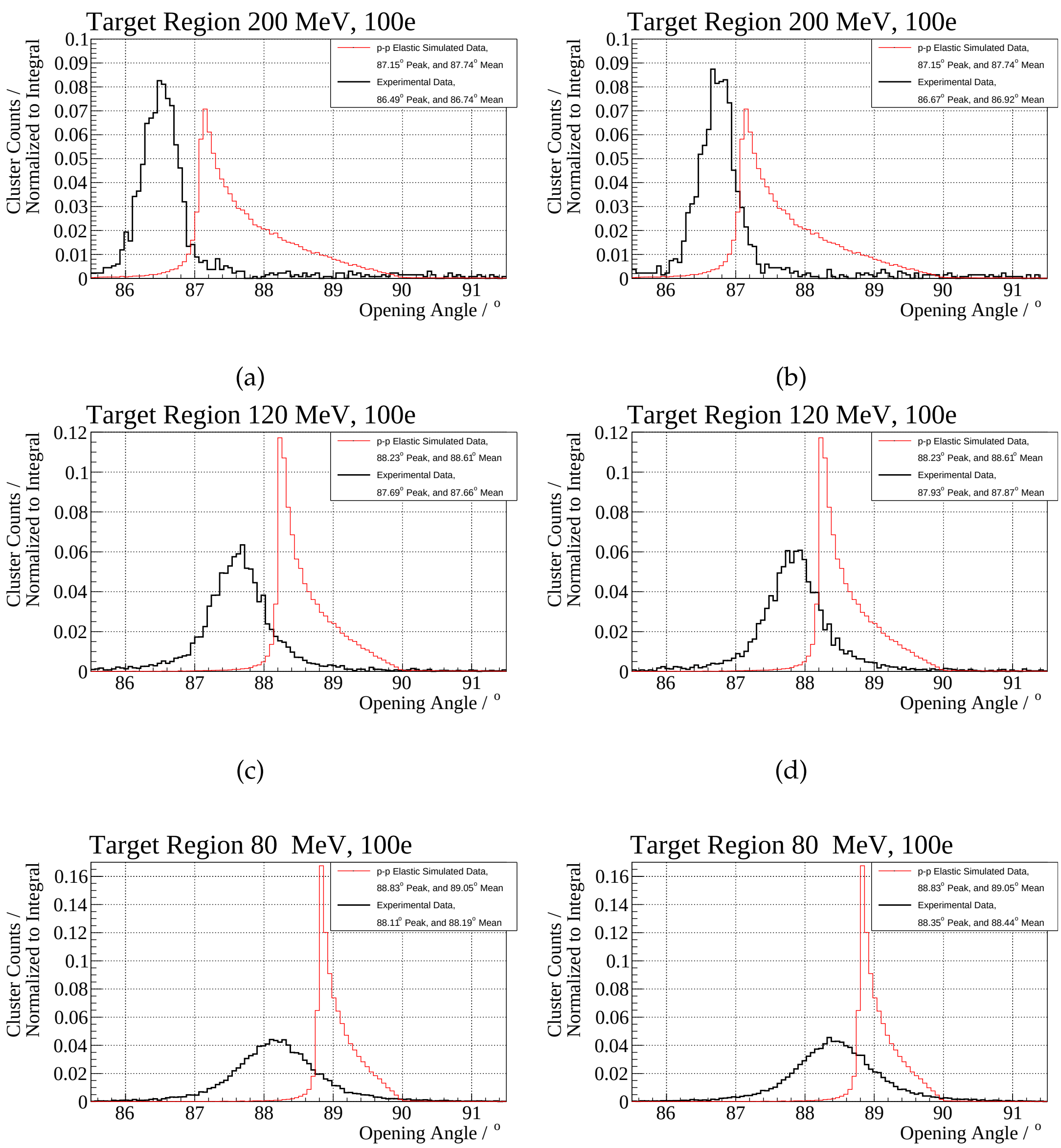

(a) (b)

(c) (d)

(e) No alignment applied (f) Alignement applied

Figure 5.2: Plots of experimental opening angles against simulated expectation for p-p elastic scattering for the three beam energies energies

6 Conclusion

After a test beam run and analysis of the results, the bent ALPIDE chips have been successfully qualified and trial many different alignment methods have been developed and examined. The first section will summarize the cluster analysis results, including the cluster size correlation with beam energy and charge threshold, and the effect of path through silicon on the cluster size. Following, the results of the alignment strategy are summarized.

6.1 Cluster Analysis Results

The clusterizing behavior in bent silicon did not bring about any undesirable surprises. The angle of incidence through the detector did not correlate with the cluster sizes. Increasing the charge collection threshold had its intended effect of reducing the cluster size and suggests the threshold's function of limiting background will not be impeded by any new challenge brought about by the bent geometry of the chips. Furthermore, while there was a correlation between the mean proton momentum, and cluster size as was expected by the Bethe-Bloch equation, the distribution of cluster sizes was rather broad and suggests that the usage of cluster size for PID or to calculate momentum is rather limited.

6.2 Alignment Results

The detector was aligned with success mostly. Track DCA improved more than an order of magnitude after alignment, where it went from about 840 µm to 50 µm, which is close to the limit imposed by multiple scattering, as simulated to be of at least 11 µm, and would increase if air scattering were implemented. From the DCA plots of the alignment applied to different beam energies, it would seem that the DCA is limited by the multiple scattering. The higher the momentum, the lower the multiple scattering angle for protons in the energy regime used. The linear relationship between momentum and DCA, implies that the physical limit on DCA calculation due to multiple scattering is not far off the 50 µm value achieved. In addition, the opening angle improved slightly when the alignment was applied. It is possible that the difference in opening angle distribution is influenced by factors other than alignment, such as quasi-free scattering with carbon.

As summarized in table 6.1, the DCA values converged for multiple different strategies, but ultimately the most promising strategy tested was the eight-dimensional bisection algorithm, in which each detector was shifted with respect to each other detector (except for one stationary anchor detector) azimuthally about the beam axis, and translationally along the beam axis. Introducing a degree of freedom in which the detector was allowed to rotate about the vertical axis, but did not improve improve DCA. It can be inferred that the technique to assemble the barrels in the μITS3 was very successful. The twelve-dimensional alignment (simultaneous eight-dimensional bisection with polar rotation) consumed significantly more computing power to yield results that did not noticeably improve from the eight-dimensional bisection alignment.

Method	$\langle$**DCA** $\rangle$ **/ [µm]**	**Median DCA / [µm]**	$\langle\theta_{Opening}\rangle$ **/ [°]**	**Time / [Hrs.]**
No Alignment	835.251	832.128	86.56252	-
Kinematic Constraint	55.7	72.9	86.57	10^{-3}
Single Detector	61.744	79.832	83.5395	0.1
8D A-0 Anchor	54.178	72.821	86.58901	0.7
8D A-1 Anchor	55.155	72.809	86.11674	0.7
8D Twist A-0 Anchor	54.474	72.797	86.59037	0.9
8D Twist A-1 Anchor	54.989	72.808	86.12204	0.9
12D Twist	54.965	72.276	86.5885	10
Machine Learning[1]	868.105	867.526	84.32139	10

Table 6.1: Table of alignment results using the hardest cuts detailed in chapter 4, for different alignment strategies used, the data to reach the values used in this table come from a 200 MeV data file, so the opening angle should be ideally 87.08°. As mentioned in chapter 5, the higher energy beam provides cleaner tracks, so naturally, it was chosen to evaluate the quality.

[1] Machine learning is only discussed in the outlook

7 Outlook

This chapter discusses work that could be carried out to close results further. Machine Learning Alignment might be used for the future ITS "IRIS" after ITS3, and Millipede alignment, the current alignment algorithm used for ITS2. Additions that can be implemented into the multiple scattering algorithm are also elaborated on.

7.1 Multiple Scattering with Air

The DCA limit was not calculated in as much detail as it should be. Multiple scattering with air is expected to play about as much of a role as silicon, which affects the scattering angle two orders of magnitude more than multiple scatterings on the target fiber. It is likely this is why the different alignment approaches could not be improved beyond 50 µm DCA and implied by the experimental results of the lower momentum (more scattered) beam energies' DCA values under the same alignment configuration.

7.2 Millipede Alignment

Millipede alignment, the current alignment method used in ITS2, is an algorithm implemented in Corryvreckan that uses linear least squares to determine local and global parameters ranging from $\sim 10^3 - 10^4$s. Local parameters correspond to individual tracks, such as slope or curvature, whereas global parameters correspond to system alignment. Millipede alignment takes $\sim 10^3 - 10^6$ events and fits them simultaneously. For implementation into ITS3, it would need to be modified to handle bent geometries and thus was not used in this analysis conducted here. It would be interesting to run it on the test beam data to compare the performance with the developed algorithms with the current approach.

7.3 Machine Learning Alignment

Using the simulation mentioned in chapter 1 as input, a Neural Network (NN) based machine learning algorithm was also developed as an alternative alignment method. This approach is especially promising for bent detectors as it can easily be generalized to handle complicated degrees of freedom, such as the sensor not being perfectly cylindrical after bending. Furthermore, such an approach, if shown to be as accurate as other methods, can be crucial for detectors where the alignment is expected to change over time, necessitating repetitive execution of the alignment procedure. This is because, once the network is fully trained, the actual inference of the misalignment in the recorded data is very fast and computationally trivial.

An initial NN for determining the feasibility of such an approach was created within the TensorFlow framework. It features two hidden layers each featuring 50 nodes, and is used to predict the misalignment in a given dataset. The network has access only to the measured cluster positions in the local ALPIDE coordinate system and thus does not know about the used experimental geometry. During training the network is provided with abundant simulated data with introduced misalignments, where the goal is to minimize the difference between predicted misalignment from the actually applied misalignment. For the initial tests, only a misalignment in translational and rotational degrees of freedom was implemented in the simulation (as discussed in 4). During training with simulation, the performance of the NN was also judged by comparing reconstructed vertex positions to the simulation truth. In those tests, it was observed that the NN can restore the vertexing resolution down to a couple of micron levels, even in extreme test cases where all ALPIDEs were significantly (up to 1 mm) misaligned in all directions.

With this, the network was given real measured data and was used to predict the misalignment. The vertex and DCA distributions after applying an according correction are shown in 7.1. It can be observed that the sharpness of the target (in terms of vertex placement and DCA) could be improved compared to the no alignment case. However, it is not as good as what was possible to achieve using the other methods described in 4. The conducted tests successfully demonstrate the viability of a machine learning-based approach to detector alignment. Significant improvements are expected for future implementations of the neural network by improving the geometry used in the simulation and training longer with more input data. This effort is currently ongoing and more robust versions of this method are hoped to be obtained soon.

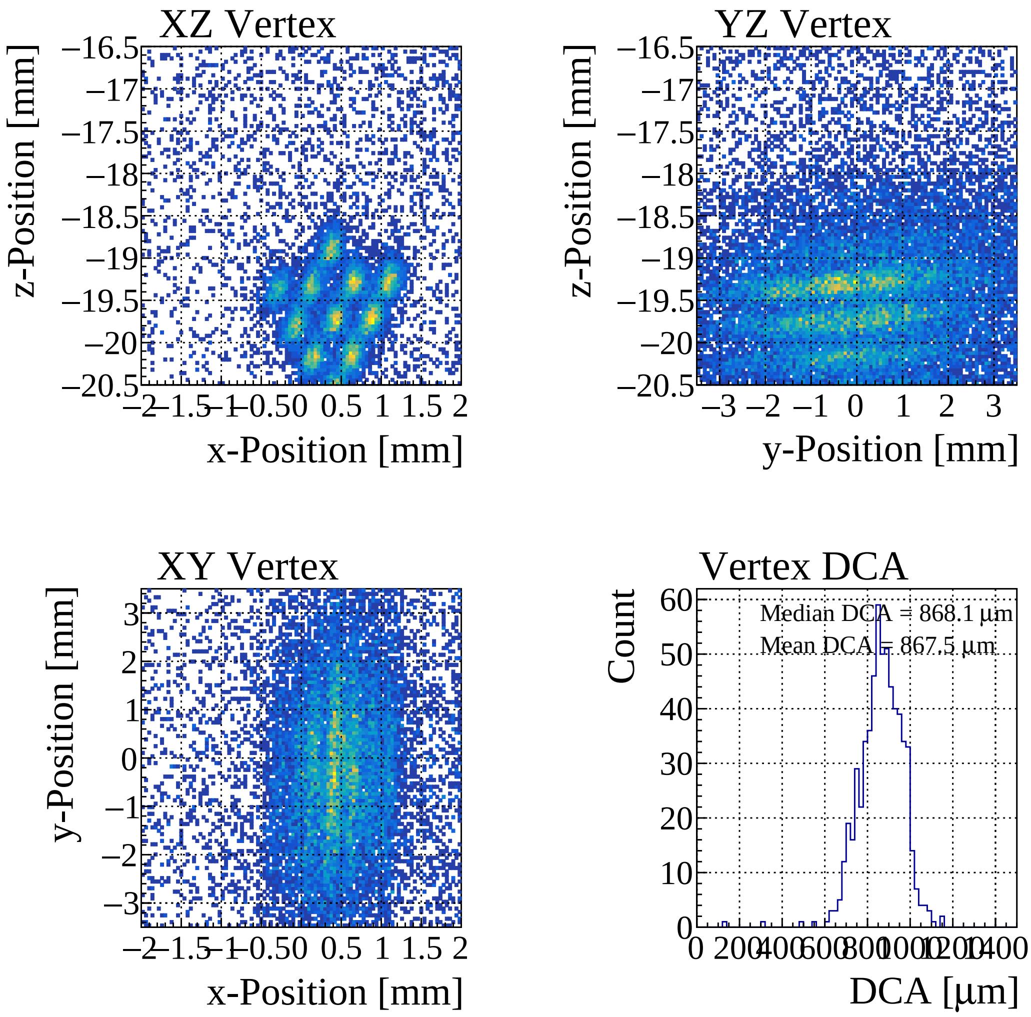

Figure 7.1: Machine Learning Alignment Result

8 Appendix

This chapter includes additional results figures mentioned but not in the main text. Here, there are figures of opening angles at 80 MeV and 120 MeV, tables of the coordinate shifts arrived at for the various alignment strategies, plots of reconstructed vertexes for different alignment strategies, and the vertex of the cleanest tracks used for alignment trials.

8.1 Opening Angle Plots

Here opening angle simulation results for proton beam energies of 200 MeV, 120 MeV, and 80 MeV are shown for p-p elastic and quasi-free scattering of p(^{12}C, ^{11}B) 2 p are shown alongside experimental results. As can be seen from the simulation in fig. 8.1, the opening angle distribution for quasi-free scattering is far broader than the p-p elastic scattering and spans the entire range from 0° to 180°. The ALPIDE detectors spanned only from 40° to 50° from the beam axis, corresponding to minimum and maximum measurable opening angles of $80^\circ - 100^\circ$. During the second weekend of test beams, the target was shifted away from the detector to accommodate the smaller opening angle originally expected to be observed. The quasi-free scattering opening angle was calculated without accounting for the contribution from the internal momentum of the target nucleon, which significantly contributes to the scattering angle such that the entire spectrum becomes diffuse, as seen in fig. 8.1. The sharp peak corresponds to the elastic p-p scattering, while the broad spectrum corresponds to the p(^{12}C, ^{11}B) 2 p channel.

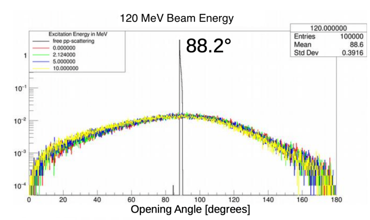

(a) Simulated 120 MeV Opening Angle Distribution

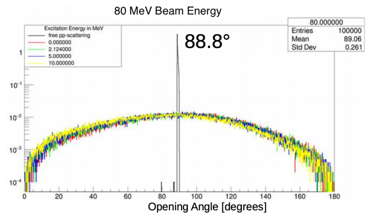

(b) Simulated 80 MeV Opening Angle Distribution

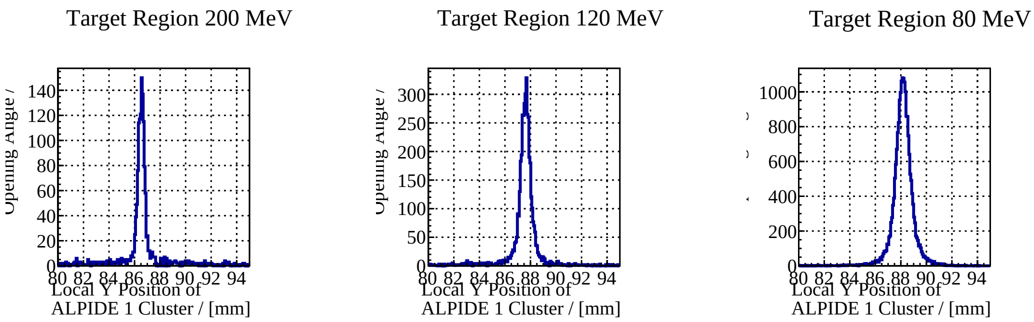

(c) Opening angles from experimental data when the target was shifted into the position where quasi-free scattering was initially expected.

Figure 8.1: Simulated distribution of opening angles at test beam energies, including quasi-free scattering and elastic scattering reaction channels at 80 MeV and 120 MeV[provided by T. Jenegger] (top) compared with experimental opening angle data (bottom)

8.2 Obtained Displacements

This section contains the determined displacements by different alignment strategies. Although the alignments do not have the same transformation value, it does not necessarily mean that the alignments position the detectors differently with respect to one another. Different detectors were held in place (anchored) for the alignment of the system. Since the remaining detectors moved with respect to the anchor detector, the resulting transformations of the system are relative to the anchor detector. However, they may still, in fact, be in the same configuration. Thus, it should be noted that for an exact comparison of the obtained values one would need to correct for global transformations.

In addition to the alignment configuration results, this section contains vertex and DCA plots of the alignments not already presented in chapter 4 or chapter 7.

Local-x Displacement / [μm]	**A 0**	**A 1**	**A 2**	**A 3**	**A 4**
No Alignment	0	0	0	0	0
Kinematic Constraint	0	1100	200	0	0
Single Detector	0	1030	0	188	0
8 Dimension A-0 Anchor	0	1105	191	9.38	4.69
8 Dim Twist A-0 Anchor	“”	“”	“”	“”	“”
8 Dimension A-1 Anchor	0	1100	200	0	0
8 Dim Twist A-1 Anchor	“”	“”	“”	“”	“”
12 Dim Twist	0	1110	199	1.17	9.38
Machine Learning	200	-743	816	-103	-422

Table 8.1: Local x Alignments

Local-y Displacement / [μm]	**A 0**	**A 1**	**A 2**	**A 3**	**A 4**
No Alignment	0	0	0	0	0
Kinematic Constraint	0	0	0	0	0
Single Detector	-1000	-969	156	188	-31.3
8 Dimension A-0 Anchor	0	14.7	4.69	-4.69	8.79
8 Dim Twist A-0 Anchor	“”	“”	“”	“”	“”
8 Dimension A-1 Anchor	-0.586	14.9	0	-3.52	-210
8 Dim Twist A-1 Anchor	“”	“”	“”	“”	“”
12 Dim Twist	0	36.9	0.293	-0.293	0.293
Machine Learning	897	898	963	-313	-1320

Table 8.2: Local y Alignments

Barrel Twists / [$^\circ \times 10^{-3}$]	**A 0**	**A 1**	**A 2**	**A 3**	**A 4**
8 Dim Twist A-0 Anchor	0	0	0	-140	0
8 Dim Twist A-1 Anchor	0.0547	0	31.2	1.40	62.5
12 Dim Twist	0	531	-0.977	-31.3	0.0303

Table 8.3: Polar Rotational Alignments (about vertical axis)

Kinematic Plane Displacement / µm	**A 0**	**A 1**	**A 2**	**A 3**	**A 4**	$\langle A \rangle$
No Alignment	-4390	4030	192	870	-1460	2190
Kinematic Constraint	-93.6	106.57	-6.4	45.20	-76.4	65.66
Single Detector	-31.9	52.87	-7.7	29.24	-47.9	33.94
8 Dimension A-0 Anchor	-59.4	67.64	-4.0	28.43	-47.6	41.43
8 Dim Twist A-0	-59.4	67.64	-4.0	28.43	-47.6	41.43
8 Dimension A-1 Anchor	-78.2	86.46	-4.1	35.28	-59.7	52.77
8 Dim Twist A-1	-78.2	86.46	-4.1	35.28	-59.7	52.77
12 Dim Twist	-61.8	63.36	-0.8	21.39	-35.9	36.68
Machine Learning	-791	-1240	1030	-2370	3980	1880

Table 8.4: Table of average kinematic displacements for each detector on the planes formed by each combination of detector planes. The final column is the average of the displacements of all ALPIDEs in an alignment configuration.

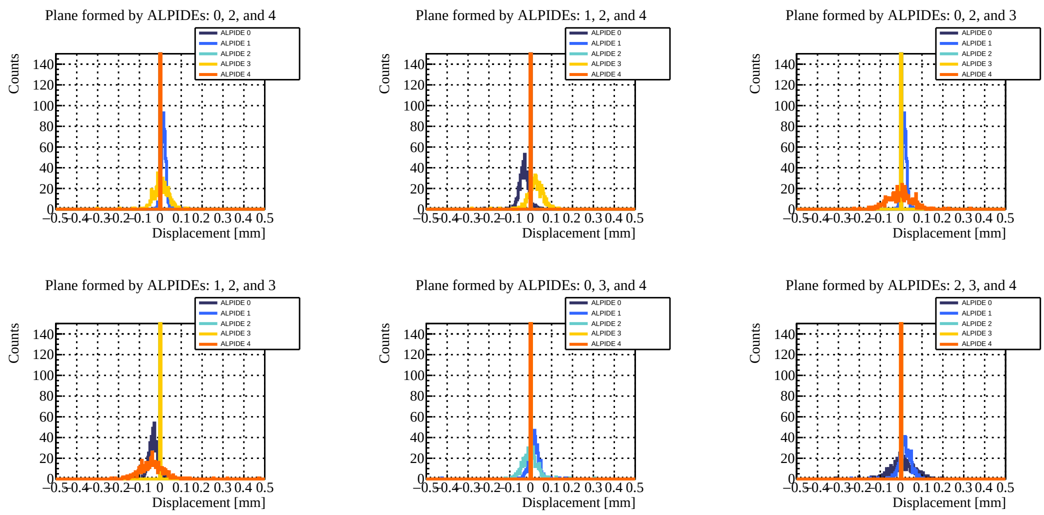

Figure 8.2: Cluster distance to planes after alignment have moved such that they are centered at zero compared to the initial displacement of detectors from the kinematic plane

8.3 Vertex Distributions

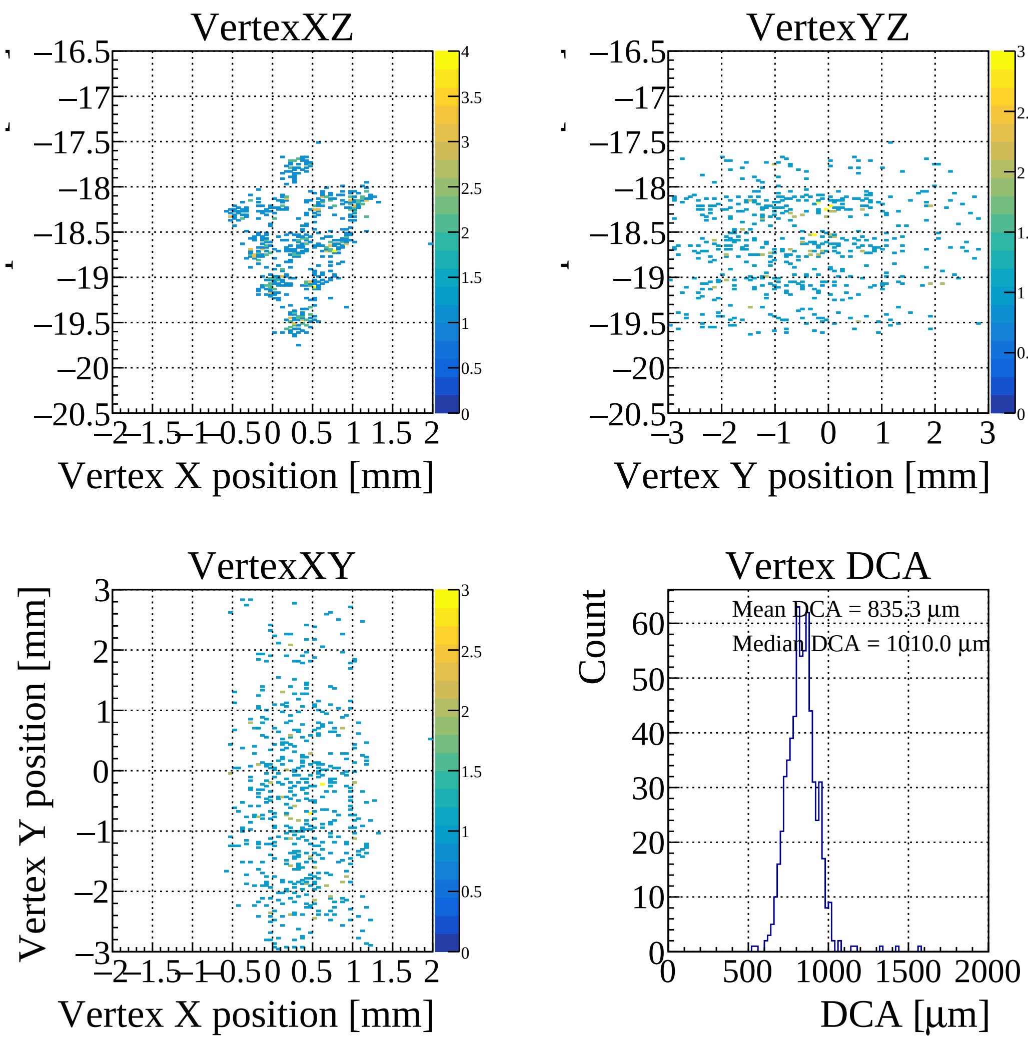

Figure 8.3: Reconstructed vertex of very clean data used to evaluate alignment strategies (without any alignment applied). Only 616 events remained after the cuts.

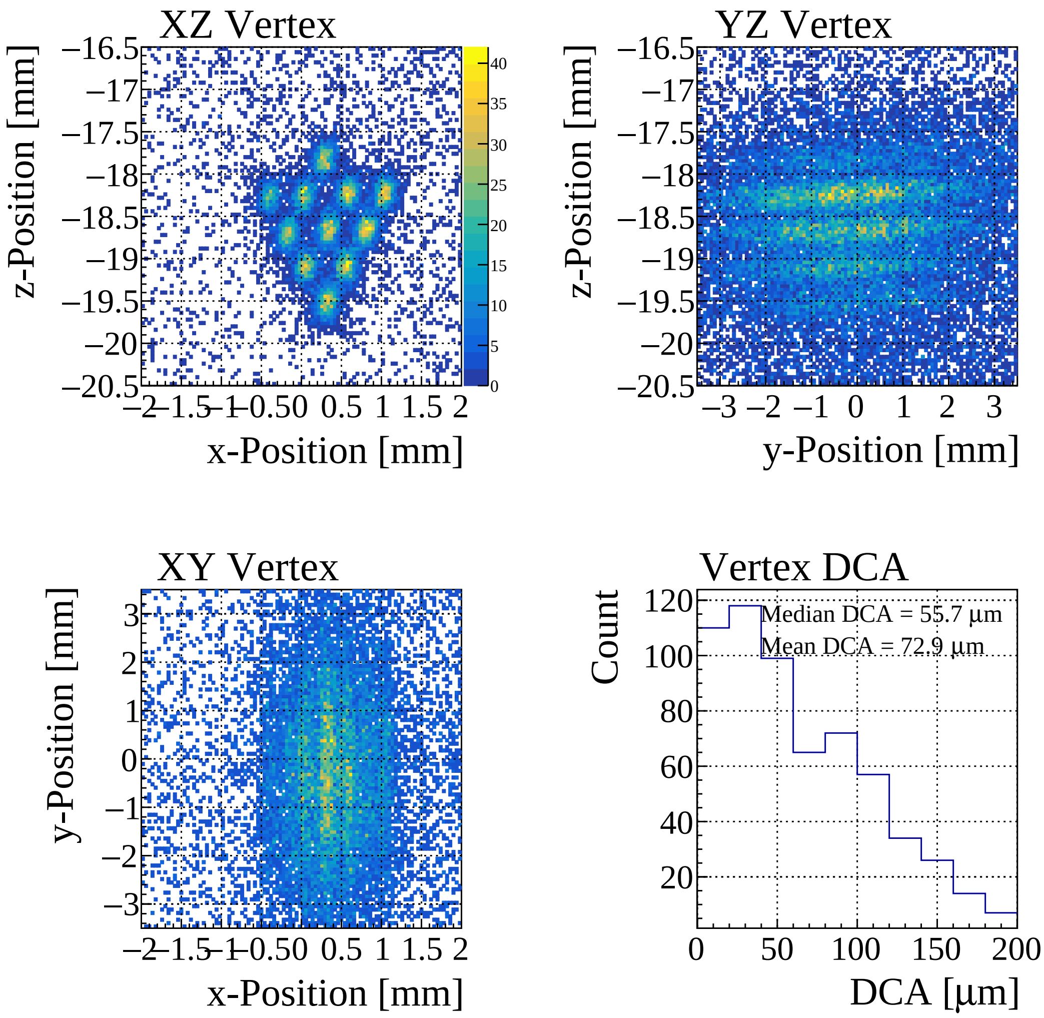

Figure 8.4: Reconstructed vertex using the kinematic constraint alignment by eye. This was essentially an instantaneous result that aligned the system very simply

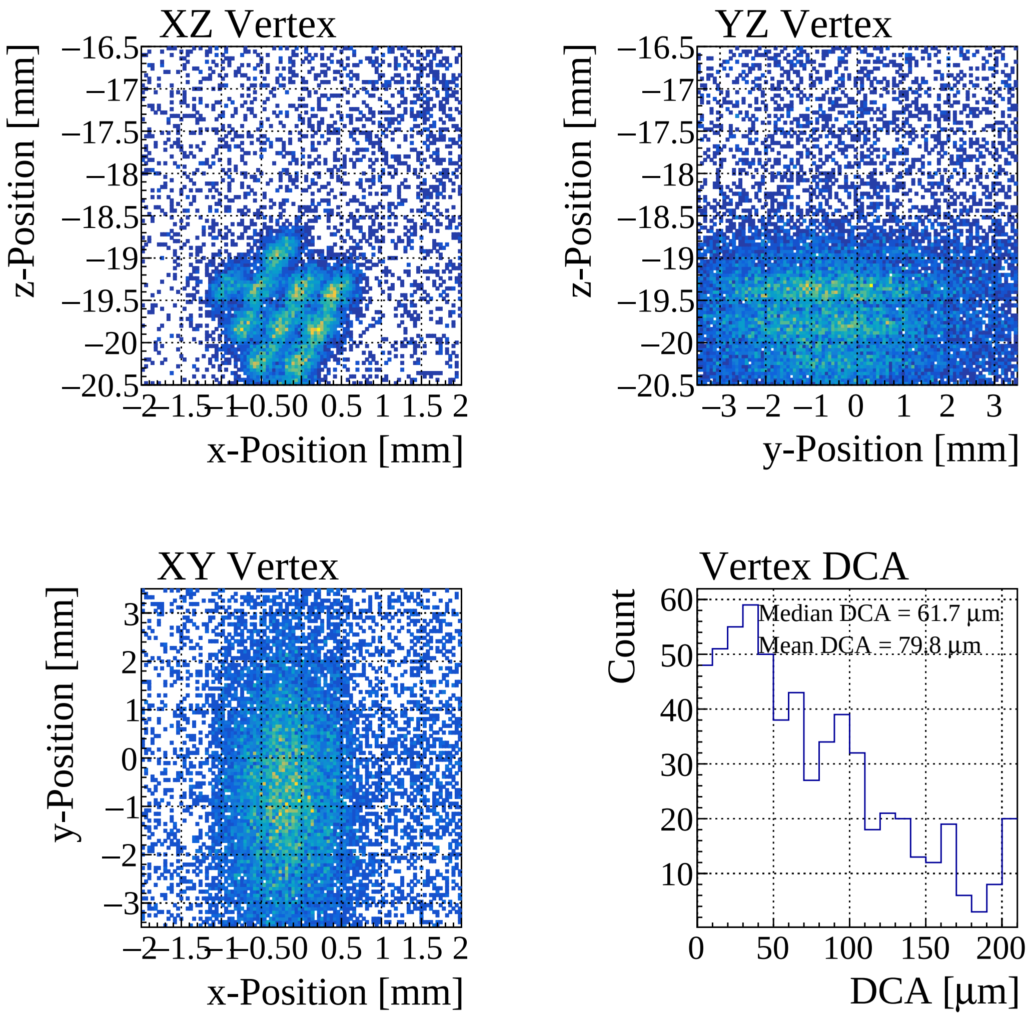

Figure 8.5: Alignment trial from one at a time detector bisection alignment

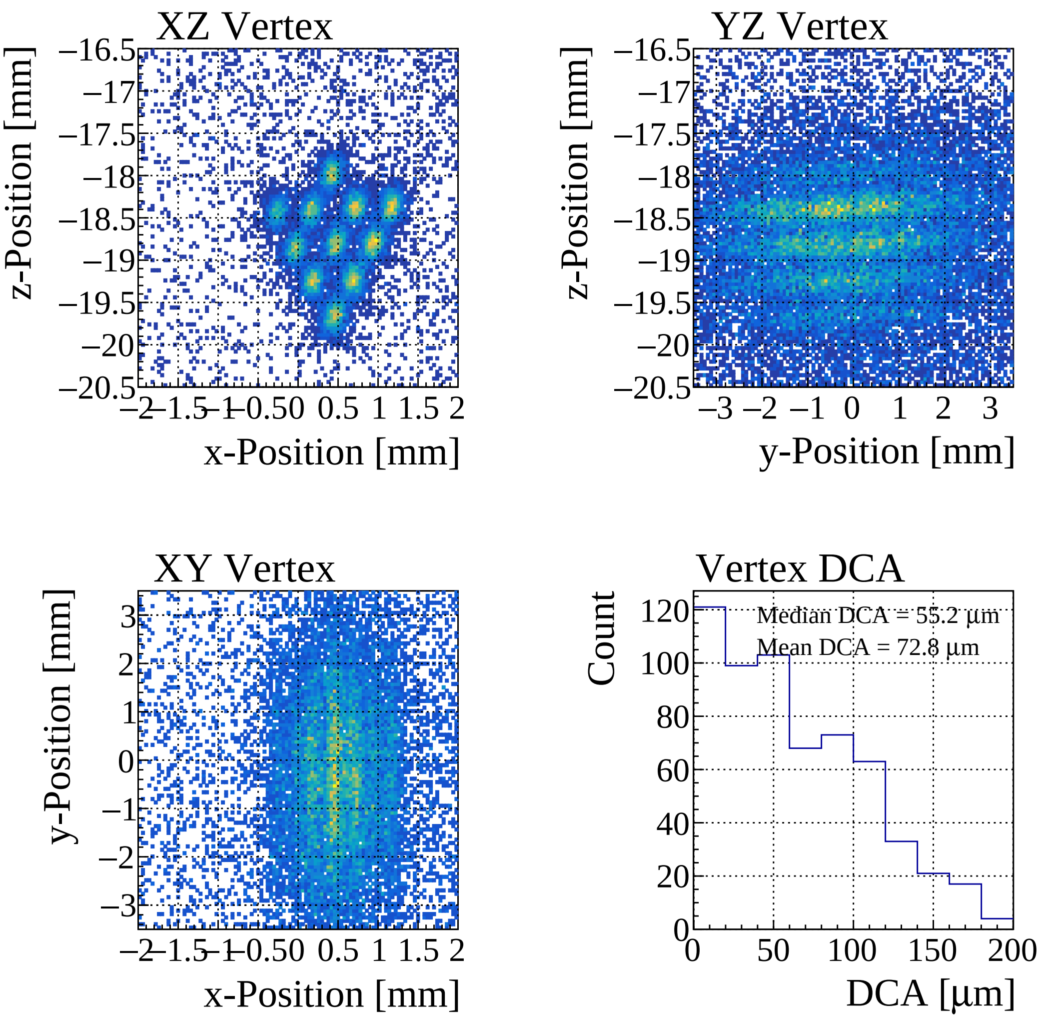

Figure 8.6: Reconstructed vertex using an eight-dimensional alignment strategy and different anchor detector (ALPIDE 1 held fixed, with ALPIDE 1 and 2 starting ranges restricted to the neighborhood of kinematic constraint found shift values). Results comparable to the alignment using ALPIDE 0 as an anchor that was plotted in chapter 4.

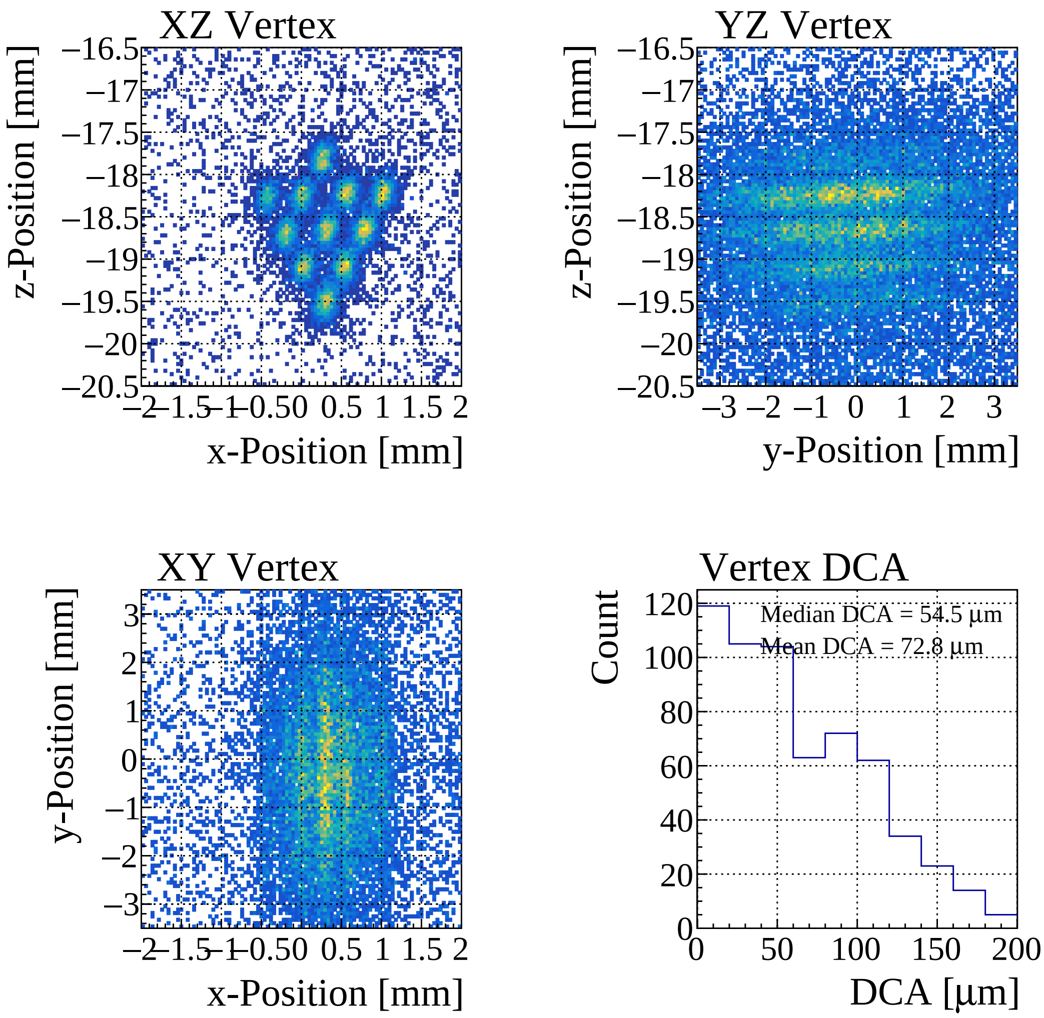

Figure 8.7: Alignment trial of barrel twist alignment, prealigned using the multiple detector bisection alignment (A-0 Fixed). The takeaway from this is that the barrels were already well-aligned and fixed securely.

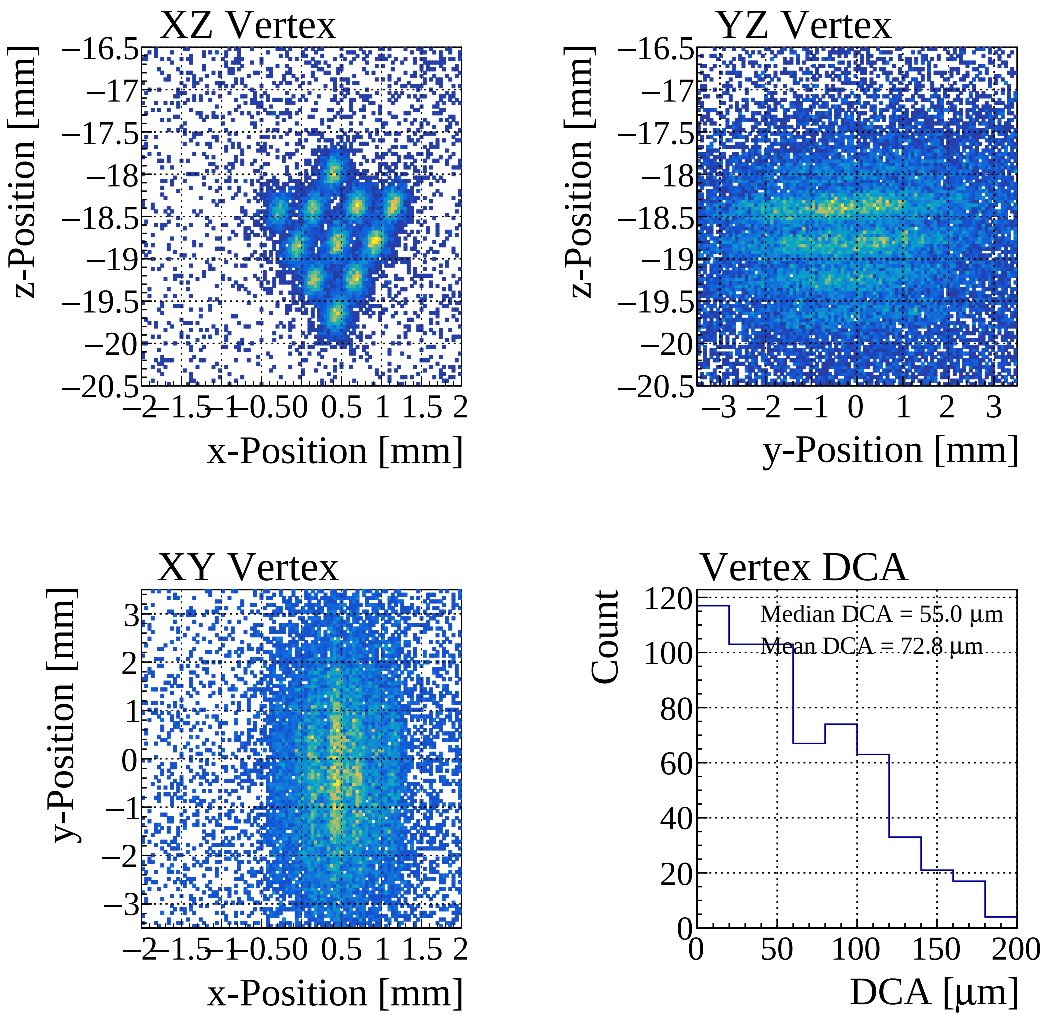

Figure 8.8: Alignment trial of barrel twist alignment, prealigned using the multiple detector bisection alignment (A1 Fixed)

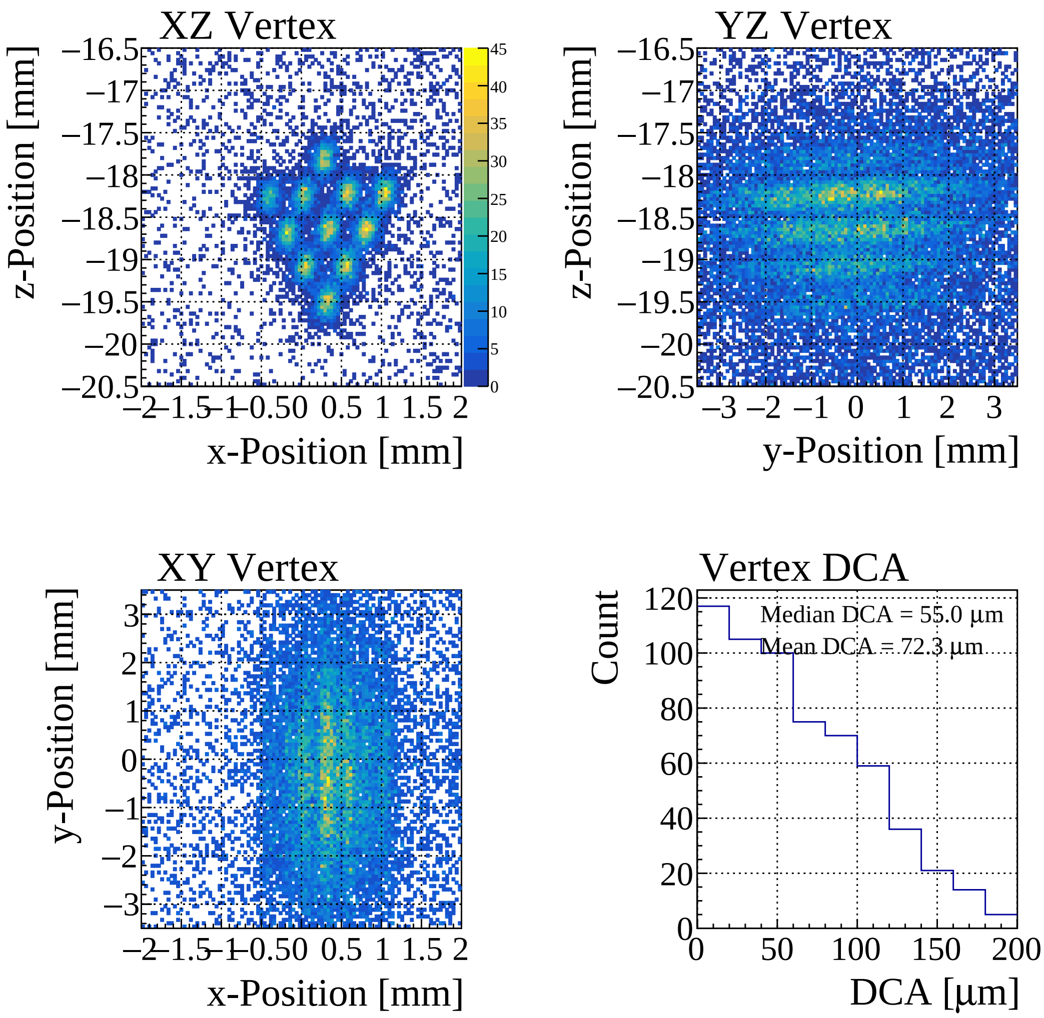

Figure 8.9: Alignment vertex with ALPIDE 0 constant, and simultaneous three dimensions free for each detector (local x, local y, and barrel twist). This consumed much more computing power to yield the same results as the eight-dimensional bisection.

Acknowledgments

Thank you to my mentors, Berkin, Laura, Roman, and Laszlo, for all of the guidance and support. Laura, you have shown me that with a sharp mind, and a burning ambition one can build a legacy. In the last year, I have learned so much from this team about how science is conducted and investigated, and thanks to you, I have achieved my goal of exploring the fascinating realm of nuclear physics by being a part of the group. I want to give a special thanks to Berkin for going way above and beyond my expectations of a mentor to guide me through the world of data analysis and teaching me not only how to become an independent researcher but also for serving as a role model for me to aspire towards what someone can achieve if they put their whole heart into it.

I want to thank my team from CNSI, too, for almost two years at the reactor. It was so much fun working in your group, getting to work on the applied side of nuclear physics in parallel to exploring the experimental realm. It has been a lifelong dream of mine to work in nuclear. Christian, you have been so inspiring to me as a boss and mentor. It has been one of my greatest privileges to work under you in such a unique and motivated team of hard-working people on the technology that excites me most.

Finally, I want to thank my family for all of the encouragement. Six years ago, with your support, I made the absurd decision to move a continent and an ocean away to begin my journey, and yet our love continues to grow tighter, and despite the challenge seems to have turned out for the best.

List of Figures

List of Tables

Bibliography

[1] R. Bruce, R. A. Fernandez, T. Argyropoulos, H. Bartosik, C. Bracco, M. D'Andrea, A. Frasca, P. Hermes, J. Jowett, D. Mirarchi, et al. *First results of running the LHC with lead ions at a beam energy of 6.8 Z TeV*.

[2] A. Collaboration et al. "Measurement of ψ (2S) production as a function of charged-particle pseudorapidity density in pp collisions at $\sqrt{s_{NN}}$= 13 TeV and p–Pb collisions at$\sqrt{sNN}$= 8.16 TeV with ALICE at the LHC". In: *Journal of High Energy Physics* 2023 (2023).

[3] A. Lopes and M. L. Perrey. *FAQ-LHC The guide*. Tech. rep. 2022.

[4] S. Fartoukh, I. Efthymiopoulos, R. Tomas Garcia, R. Bruce, H. Timko, G. Arduini, N. Mounet, Y. Papaphilippou, B. Salvant, S. Redaelli, et al. *LHC configuration and operational scenario for run 3*. Tech. rep. 2021.

[5] B. Povh, K. Rith, C. Scholz, F. Zetsche, and W. Rodejohann. "Particles and nuclei". In: *An Introduction to the Physical Concepts, Berlin and Heidelberg: Springer-Verlag (Italian Translation:(1998), Particelle e nuclei. Un'introduzione ai concetti sici, Torino: Bollati Boringhieri editore)* (1995).

[6] L. Šerkšnytė. "Novel technique to access the strong interaction in three-body systems and Re-evaluated cosmic ray antinuclei fluxes". en. PhD thesis. Technische Universität München, 2023, p. 190.

[7] R. L. Workman et al. "Review of Particle Physics". In: *PTEP* 2022 (2022), p. 083C01. DOI: `10.1093/ptep/ptac097`.

[8] D. Andreou. "Heavy Flavour measurements in Pb − Pb collisions with the upgraded ALICE Inner Tracking System". In: *arXiv preprint arXiv:2004.14877* (2020).

[9] W. Poonsawat, C. Kobdaj, M. Sitta, and Y. Yan. "Stave module design and development of the new ALICE Inner Tracking System". In: *Journal of Instrumentation* 14.05 (2019), P05003.

[10] R. Lemmon. "The ALICE Inner Tracking System Upgrade". In: *Nuclear Physics A* 904-905 (2013). The Quark Matter 2012, pp. 937c–940c. ISSN: 0375-9474. DOI: `https://doi.org/10.1016/j.nuclphysa.2013.02.169`. URL: `https://www.sciencedirect.com/science/article/pii/S0375947413002959`.

[11] L. Musa. *Conceptual Design Report for the Upgrade of the ALICE ITS*. Tech. rep. Geneva: CERN, 2012. URL: `https://cds.cern.ch/record/1431539`.

[12] A. Tauro. "ALICE Schematics". General Photo. 2017. URL: `https://cds.cern.ch/record/2263642`.

[13] E. Botta. *Particle identification performance at ALICE. Particle identification performance at ALICE*. Tech. rep. 6 pages, 5 figures, Proceeding of the Fifth Annual Conference on Large Hadron Collider Physics, May 15-20, 2017, Shanghai, Cina. 2017. arXiv: 1709.00288. URL: https://cds.cern.ch/record/2282027.

[14] B. A. et al and (. A. Collaboration). "Technical Design Report for the Upgrade of the ALICE Inner Tracking System". In: *Journal of Physics G: Nuclear and Particle Physics* 41.8 (July 2014), p. 087002. DOI: 10.1088/0954-3899/41/8/087002. URL: https://dx.doi.org/10.1088/0954-3899/41/8/087002.

[15] L. Musa. *Letter of Intent for an ALICE ITS Upgrade in LS3*. Tech. rep. Geneva: CERN, 2019. DOI: 10.17181/CERN-LHCC-2019-018. URL: https://cds.cern.ch/record/2703140.

[16] N. W. Ashcroft and N. D. Mermin. *Solid state physics*. Cengage Learning, 2022.

[17] M. Šuljić. "ALPIDE: the Monolithic Active Pixel Sensor for the ALICE ITS upgrade". In: *Journal of Instrumentation* 11.11 (Nov. 2016), p. C11025. DOI: 10.1088/1748-0221/11/11/C11025. URL: https://dx.doi.org/10.1088/1748-0221/11/11/C11025.

[18] L. Greiner. "MAPS application in the STAR and ALICE experiments". In: *Nuclear Instruments and Methods in Physics Research Section A: Accelerators, Spectrometers, Detectors and Associated Equipment* 942 (2019), p. 162283.

[19] F. Reidt. "Upgrade of the ALICE ITS detector". In: *Nuclear Instruments and Methods in Physics Research Section A: Accelerators, Spectrometers, Detectors and Associated Equipment* 1032 (June 2022), p. 166632. DOI: 10.1016/j.nima.2022.166632. URL: https://doi.org/10.1016%2Fj.nima.2022.166632.

[20] A. Yüncü. *A truly cylindrical inner tracker for ALICE*. 2022. arXiv: 2212.03165 [physics.ins-det].

[21] N. Apadula, W. Armstrong, J. Brau, M. Breidenbach, R. Caputo, G. Carinii, A. Collu, M. Demarteau, G. Deptuch, A. Dragone, G. Giacomini, C. Grace, N. Graf, L. Greiner, R. Herbst, G. Haller, M. Jadhav, S. Joosten, C. J. Kenney, C. Kierans, J. Kim, T. Markiewicz, Y. Mei, J. Metcalfe, Z.-E. Meziani, T. K. Nelson, C. Peng, G. Pinaroli, P. E. Reimer, L. Rota, M. Scott, J. Segal, E. Sichterman, N. Sinev, A. Steinhebel, D. Strom, A. Tricoli, C. Vernieri, C. Young, and M. Zurek. *Monolithic Active Pixel Sensors on CMOS technologies*. 2022. arXiv: 2203.07626 [physics.ins-det].

[22] R. Turchetta, A. Fant, P. Gasiorek, C. Esbrand, J. Griffiths, M. Metaxas, G. Royle, R. Speller, C. Venanzi, P. van der Stelt, H. Verheij, G. Li, S. Theodoridis, H. Georgiou, D. Cavouras, G. Hall, M. Noy, J. Jones, J. Leaver, D. Machin, S. Greenwood, M. Khaleeq, H. Schulerud, J. Østby, F. Triantis, A. Asimidis, D. Bolanakis, N. Manthos, R. Longo, and A. Bergamaschi. "CMOS Monolithic Active Pixel Sensors (MAPS): Developments and future outlook". In: *Nuclear Instruments and Methods in Physics Research Section A: Accelerators, Spectrometers, Detectors and Associated Equipment* 582.3 (2007). VERTEX 2006, pp. 866–870. ISSN: 0168-9002. DOI: https://doi.org/10.1016/j.nima.2007.07.112. URL: https://www.sciencedirect.com/science/article/pii/S0168900207015896.

[23] G. Contin. "The MAPS-based ITS Upgrade for ALICE". In: *Proceedings of The 28th International Workshop on Vertex Detectors — PoS(Vertex2019)*. Vol. 373. 2020, p. 003. DOI: 10.22323/1.373.0003.

[24] I. ALICE. "ALPIDE development team". In: *Alpide operations manual* 2.8 (2016), p. 3.

[25] J. Iddon. "Construction, Commissioning and Performance Measurements of the Inner Tracking System Upgrade (ITS2) of ALICE at the LHC". In: (2022). DOI: 10.17638/03163867. URL: https://livrepository.liverpool.ac.uk/id/eprint/3163867.

[26] J. Schambach, M. Rossewij, K. Sielewicz, G. A. Rinella, M. Bonora, J. Ferencei, P. Giubilato, and T. Vanat. "ALICE inner tracking system readout electronics prototype testing with the CERN"Giga Bit Transceiver"". In: *Journal of Instrumentation* 11.12 (2016), p. C12074.

[27] M. Keil. "Upgrade of the ALICE Inner Tracking System". In: *Journal of Instrumentation* 10.03 (Mar. 2015), p. C03012. DOI: 10.1088/1748-0221/10/03/C03012. URL: https://dx.doi.org/10.1088/1748-0221/10/03/C03012.

[28] V. Panin, T. Aumann, and C. Bertulani. "Quasi-free scattering in inverse kinematics as a tool to unveil the structure of nuclei: A tribute to Mahir S. Hussein". In: *The European Physical Journal A* 57 (2021), pp. 1–13.

[29] K. Riley. "C12(p, 2p)B11 in the impulse approximation". In: *Nuclear Physics* 13.3 (1959), pp. 407–419. ISSN: 0029-5582. DOI: https://doi.org/10.1016/0029-5582(59)90118-X. URL: https://www.sciencedirect.com/science/article/pii/002955825990118X.

[30] V. Panin, J. Taylor, S. Paschalis, F. Wamers, Y. Aksyutina, H. Alvarez-Pol, T. Aumann, C. Bertulani, K. Boretzky, C. Caesar, M. Chartier, L. Chulkov, D. Cortina-Gil, J. Enders, O. Ershova, H. Geissel, R. Gernhäuser, M. Heil, H. Johansson, B. Jonson, A. Kelić-Heil, C. Langer, T. Le Bleis, R. Lemmon, T. Nilsson, M. Petri, R. Plag, R. Reifarth, D. Rossi, H. Scheit, H. Simon, H. Weick, and C. Wimmer. "Exclusive measurements of quasi-free proton scattering reactions in inverse and complete kinematics". In: *Physics Letters B* 753 (2016), pp. 204–210. ISSN: 0370-2693. DOI: https://doi.org/10.1016/j.physletb.2015.11.082. URL: https://www.sciencedirect.com/science/article/pii/S0370269315009612.

[31] J. Kröger, S. Spannagel, and M. Williams. "User manual for the Corryvreckan test beam data reconstruction framework, Version 1.0". In: *arXiv preprint arXiv:1912.00856* (2019).

[32] D. Dannheim, K. Dort, L. Huth, D. Hynds, I. Kremastiotis, J. Kröger, M. Munker, F. Pitters, P. Schütze, S. Spannagel, T. Vanat, and M. Williams. "Corryvreckan: a modular 4D track reconstruction and analysis software for test beam data". In: *Journal of Instrumentation* 16.03 (Mar. 2021), P03008. DOI: 10.1088/1748-0221/16/03/P03008. URL: https://dx.doi.org/10.1088/1748-0221/16/03/P03008.

[33] M. Ivanov. *RootInteractive*. URL: https://github.com/miranov25/RootInteractive.

[34] Bokeh Development Team. *Bokeh: Python library for interactive visualization*. 2018. URL: https://bokeh.pydata.org/en/latest/.

[35] H. Bethe. “Bremsformel für elektronen relativistischer geschwindigkeit”. In: *Zeitschrift für Physik* 76.5-6 (1932), pp. 293–299.

[36] S. Seltzer. *Stopping-Powers and Range Tables for Electrons, Protons, and Helium Ions, NIST Standard Reference Database 124*. en. 1993. DOI: 10.18434/T4NC7P. URL: http://www.nist.gov/pml/data/star/index.cfm.

[37] V. L. Highland. “Some practical remarks on multiple scattering”. In: *Nuclear Instruments and Methods* 129.2 (1975), pp. 497–499. ISSN: 0029-554X. DOI: https://doi.org/10.1016/0029-554X(75)90743-0. URL: https://www.sciencedirect.com/science/article/pii/0029554X75907430.

[38] P. D. Group. *Atomic and Nuclear Properties*. 2020. URL: https://pdg.lbl.gov/2020/AtomicNuclearProperties/.